Static stiffness of rigid foundation resting on elastic half-space using a Galerkin boundary element method

Daniele BARALDI[a], Nerio TULLINI[b]

[a] corresponding author; Università IUAV di Venezia, Italy; e-mail: danielebaraldi@iuav.it

[b] Department of Engineering; University of Ferrara, Italy; e-mail: nerio.tullini@unife.it

ABSTRACT

In this work, a simple and effective numerical model is proposed for studying flexible and rigid foundations in bilateral and frictionless contact with a three-dimensional elastic half-space. For this purpose, a Galerkin Boundary Element Method for the substrate is introduced, and both surface vertical displacements and half-space tractions are discretized by means of a piecewise constant function. The work focuses on a transversely isotropic substrate having the plane of isotropy parallel to the half-space boundary, hence the relationship between vertical displacements and half-space reactions is given by Michell solution, reducing to Boussinesq solution for an isotropic half-space. Several numerical tests are performed for showing the effectiveness of the model, on one hand by determining vertical displacements of flexible rectangular foundations subjected to vertical pressures, on the other hand by accurately determining the translational and rotational stiffness of rigid rectangular and L-shaped foundations. Particular attention is given to the determination of the center of stiffness in case of unsymmetrical foundations, since it turns out to be not coincident with foundation area centroid.

Keywords: Flat punch; Bilateral frictionless contact; Galerkin boundary element method.

1. INTRODUCTION

The three-dimensional (3D) elastic half-space can be considered an accurate physical model for describing the behavior of a semi-infinite linear elastic and homogeneous continuum, which can be adopted, for instance in the civil engineering field, for studying the response of a soil media subjected to external loads or displacements transmitted by flexible or rigid foundations. In this field, the use of a continuum model is accurate since it considers surface deflections arising both under the directly loaded regions, both within certain areas outside the loaded regions, as the common experience can suggest [1]. In most of real-life case studies, soil media exhibits anisotropic properties due to layering or stratification, requiring the adoption of a homogeneous, linear elastic and transversely isotropic half-space [2, 3]. Furthermore, continuum model can also be adopted in the mechanical engineering field for studying composites and surface coatings [4, 5, 6]. For these reasons, the linear elastic and transversely isotropic half-space was studied by many authors [7, 8, 9, 10, 11, 12]. Focusing on the homogeneous linear elastic and isotropic half-space, which can be assumed as a simpler model for representing half-space behavior in soil and rock mechanics [1, 13], the pioneering works of Cerruti [14] and Boussinesq [13] introduced the potential of a 3D linear elastic and isotropic half-space, which allowed to obtain the expressions of stresses and displacements generated by a concentrated force tangential and normal to the half-space surface [15], respectively. Many researchers in the past focused on the determination of the displacements generated by various force distributions on half-space surface [1]. Among the others, Lamb [16] studied the problem in cylindrical coordinates, whereas Love [17] determined the expression of half-space surface displacements generated by a uniform pressure over a rectangular area. The determination of pressures and displacements generated by rigid foundations on the half-space represents another problem involving Boussinesq solution. Many researchers determined the solution of the indentation of the rigid footing or punch problem by adopting different approaches such as power series, the Finite Element Method (FEM) or the Boundary Element Method (BEM)

[18, 19, 20, 21, 22, 23, 24, 25]. A resume of some numerical and analytical solutions of problems related to half-space surface loaded by flexible and rigid foundations can be also found in the books by Poulos and Davis [26] and Selvadurai [1]. Moreover, this problem is strictly related to the determination of the dynamic stiffness of a rigid foundation resting on an elastic soil [27, 28], and it is also a classical problem in physics, since its solution represents the charge density of a thin electrified plate [29, 30]. Furthermore recently, a renewed interest on the determination of stresses generated by half-space surface loadings over polygonal domains has been carried on by Marmo and co-workers [31, 32], with particular attention to L-shaped foundations.

In this work, a Galerkin Boundary Element Method (GBEM) is adopted for studying the behavior of flexible and rigid foundations in bilateral and frictionless contact with a 3D elastic and transversely isotropic half-space having the plane of isotropy parallel to the half-space boundary, with particular attention to the determination of the static stiffness of the rigid foundations. The proposed numerical model is based on a mixed variational formulation that assumes half-space surface vertical displacements and normal tractions in the contact region as independent fields. Such fields are numerically approximated by means of piecewise constant functions defined in the contact region of the half-space boundary only. For the sake of simplicity, the contact region is subdivided into rectangular portions.

The proposed numerical approach has been recently used to study the in-plane bending of Timoshenko beams in bilateral frictionless contact with an elastic isotropic half-space making use of a Finite Element-Boundary Integral Equation (FE-BIE) method [33], allowing to obtain fast and accurate results in terms of beam displacements and contact tractions. The FE-BIE method was extensively used with elastic two-dimensional substrate, e.g., in the static analysis of Timoshenko beams and frames in frictionless [34, 35] or fully adhesive [36, 37] contact with an half-plane, and also to study bars and thin coatings [38, 39]. Moreover, the FE-BIE coupling method was also used to analyze the buckling of Euler-Bernoulli [40, 41] and Timoshenko [42] beams in bilateral frictionless contact with an elastic half-plane. In all these studies, the numerical performance of the FE-BIE coupling method shown an excellent convergence rate in comparison with those of other standard numerical methods.

Differently by the classical FEM-BEM approach based on collocation BEM, which requires an additional computational effort to remedy the lack of symmetry of the BEM coefficient matrix, the proposed GBEM involves a symmetric substrate matrix, Additionally, in the present study the weakly singular BIE is evaluated analytically, so avoiding singular and hyper-singular integrals, that are the major concern of the classical BEM. Moreover, the resolving matrix has dimensions proportional to the number of the rigid foundation FEs. Conversely, in the standard FEM, a refined mesh requires a stiffness matrix with dimensions that are several times the square of the number of FEs used for the rigid footing. Finally, the proposed GBEM allows to set the global equilibrium equations in a proper variational framework. This aspect will be particularly suitable in the structure-footing-soil interaction problem that will be studied in forthcoming works by making use of the FE-BIE method. The advantages outlined result in accurate solutions at low computational cost.

The proposed variational formulation and the corresponding numerical model is formulated for foundations having an arbitrary shape and particular attention is given to the determination of the stiffness matrix of the rigid foundation-substrate system. The stiffness parameters are accurately determined with a small computational effort and turn out to be in excellent agreement with existing numerical solutions. Furthermore, in case of unsymmetrical rigid foundations, it is demonstrated that the center of stiffness does not coincide with the foundation centroid, as it was originally pointed out by Conway and Farnham [20].

The work is organized as follows. Considering a transversely isotropic half-space with the plane of isotropy parallel to the half-space boundary, the variational formulation of the rigid foundation-substrate system problem is provided and suitable equivalent elastic moduli are introduced to reduce the problem to the isotropic case. Then, the corresponding numerical model is detailed for the case of a flexible foundation loaded by vertical pressures and for the case of rigid foundations with prescribed vertical displacements. Particular attention is given to the definition of the stiffness matrix of the rigid foundation-substrate system. Finally, several numerical tests regarding rectangular flexible foundations and rectangular and L-shaped rigid foundations are proposed for highlighting the effectiveness of the numerical model.

2. VARIATIONAL FORMULATION

A flat foundation resting in bilateral frictionless contact with a semi-infinite substrate is referred to a Cartesian coordinate system (0; x , y , z), where the x–y plane defines the boundary of the half-space, whereas z is chosen in the downward transverse direction (Fig. 1). The foundation is subjected to a distribution of vertical loads $p(x, y)$ on the surface Ω.

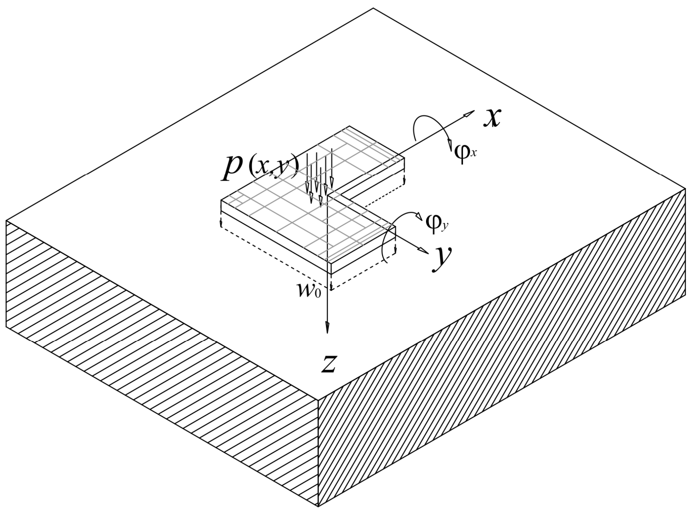

Fig. 1. Flat foundation resting on an elastic half-space.

According to Voigt compact notation, for a transversely isotropic material having the z-axis normal to the plane of isotropy, the stress–strain relationship reduces to [9, 10]

$$\begin{Bmatrix}\sigma_{xx}\\ \sigma_{yy}\\ \sigma_{zz}\\ \tau_{xz}\\ \tau_{zx}\\ \tau_{xy}\end{Bmatrix}=\begin{bmatrix}C_{11} & C_{12} & C_{13} & 0 & 0 & 0\\ C_{12} & C_{11} & C_{13} & 0 & 0 & 0\\ C_{13} & C_{13} & C_{33} & 0 & 0 & 0\\ 0 & 0 & 0 & C_{44} & 0 & 0\\ 0 & 0 & 0 & 0 & C_{44} & 0\\ 0 & 0 & 0 & 0 & 0 & \left(C_{11}-C_{12}\right)/2\end{bmatrix}\begin{Bmatrix}\varepsilon_{xx}\\ \varepsilon_{yy}\\ \varepsilon_{zz}\\ \gamma_{yz}\\ \gamma_{zx}\\ \gamma_{xy}\end{Bmatrix} \quad (1)$$

and the elastic constants can be written in terms of the engineering constants

$$C_{11}=E_x(1-\nu_{xz}\nu_{zx})\big/[(1+\nu_{xy})\,(1-\nu_{xy}-2\nu_{zx}\nu_{xz})], \quad (2a)$$

$$C_{33}=E_z(1-\nu_{xy})\big/(1-\nu_{xy}-2\nu_{zx}\nu_{xz}), \quad (2b)$$

$$C_{12}=E_x(\nu_{xy}+\nu_{xz}\nu_{zx})\big/[(1+\nu_{xy})\,(1-\nu_{xy}-2\nu_{zx}\nu_{xz})], \quad (2c)$$

$$C_{13}=E_x\nu_{zx}\big/(1-\nu_{xy}-2\nu_{zx}\nu_{xz}), \quad (2d)$$

$$C_{44}=G_{zx}, \quad (2e)$$

$$C_{66}=\left(C_{11}-C_{12}\right)/2, \quad (2f)$$

where E_z denotes Young's modulus along the vertical direction z, whereas the transverse directions x and y share the same Young's modulus E_x, G_{ij} and ν_{ij} are the shear modulus and Poisson's coefficient, respectively, associated with the pair directions i, $j = x$, y, z. In particular, due to this special kind of material symmetry, $\nu_{ij}/E_i = \nu_{ji}/E_j$.

Positive definiteness of the strain energy function of a transversely isotropic material requires [9, 10]:

$$C_{11}>0,\; C_{33}>0,\; C_{44}>0,\; 2C_{66}=C_{11}-C_{12}>0,\; C_{11}+C_{12}>0,\; (C_{11}+C_{12})\,C_{33}-2C_{13}^2>0, \quad (3)$$

The three-dimensional problem for a homogeneous, linear elastic and transversely isotropic half-space loaded by a point force normal to its boundary plane has been treated by many authors, see [7, 8, 9, 10, 11, 12] and references cited therein. In particular, the vertical displacement w of a point on the half-space boundary due to a generic normal traction $r(\xi, \eta)$ over a surface Ω is given by

$$w(x,y,0)=\frac{1}{\pi E_s}\int_\Omega \frac{r(\xi,\eta)\,\mathrm{d}\xi\,\mathrm{d}\eta}{d(x,y;\xi,\eta)} \quad (4)$$

where

$$d(x,y;\xi,\eta)=\sqrt{(x-\xi)^2+(y-\eta)^2} \tag{5}$$

is the distance between the points (x, y, 0) and (ξ,η, 0), whereas, after some algebraic manipulation of Eqs. (7.1.14) and (7.1.15) reported in [10], the equivalent elastic moduli E_s along the vertical direction z and E_t in the isotropic plane can be written as:

$$E_s=E_t\sqrt{\frac{C_{44}\left(\sqrt{C_{11}C_{33}}-C_{13}\right)}{C_{11}\left(E_t/2+2C_{44}\right)}}, \tag{6a}$$

$$E_t=2\left(\sqrt{C_{11}C_{33}}+C_{13}\right) \tag{6b}$$

It is worth remember that Eq. (6a) was first shown in [7]. It can be easily verified that both E_s and E_t are positive for all kind of transversely isotropic materials. In fact, Eq. (3d) gives $C_{11} > C_{12}$, which implies $2C_{11} > C_{11} + C_{12}$ so that also $2C_{11}\, C_{33} > (C_{11} + C_{12})\, C_{33}$; consequently, making use of Eq. (3f), it is straightforward to verify that $\sqrt{C_{11}C_{33}}-C_{13} > 0$ and $\sqrt{C_{11}C_{33}}+C_{13} > 0$. It is worth remarking that, for an isotropic substrate, the equivalent elastic moduli E_s, E_t reduce to $E_{\text{soil}}/(1-\nu_{\text{soil}}^2)$ and $2E_{\text{soil}}/[(1+\nu_{\text{soil}})(1-2\nu_{\text{soil}})]$, respectively, E_{soil} and ν_{soil} being Young's modulus and Poisson ratio of the isotropic substrate; correspondingly, Eq. (4) reduces to Boussinesq solution [9, 15].

Horizontal displacement u and v of a point on half-space boundary are given by

$$u(x,y,0)=-\frac{1}{\pi E_t}\int_\Omega \frac{(x-\xi)\, r(\xi,\eta)\,\mathrm{d}\xi\,\mathrm{d}\eta}{d(x,y;\xi,\eta)} \tag{7a}$$

$$v(x,y,0)=-\frac{1}{\pi E_t}\int_\Omega \frac{(y-\eta)\, r(\xi,\eta)\,\mathrm{d}\xi\,\mathrm{d}\eta}{d(x,y;\xi,\eta)}. \tag{7b}$$

Due to the theorem of work and energy for exterior domains [43], the strain energy of the substrate is

$$U_s(r,w)=\frac{1}{2}\int_\Omega r(x,y)\, w(x,y,0)\,\mathrm{d}x\,\mathrm{d}y. \tag{8}$$

Making use of Eq. (4), Eq. (8) becomes

$$U_s(r) = \frac{1}{2\,\pi\,E_s} \int_\Omega r(x,y)\,\mathrm{d}\,x\,\mathrm{d}\,y \int_\Omega \frac{r(\xi,\eta)\,\mathrm{d}\,\xi\,\mathrm{d}\,\eta}{d(x,y;\xi,\eta)} \tag{9}$$

The potential energy of the substrate Π_s can be written as

$$\Pi_s(r,w) = U_s(r,w) - \frac{1}{2}\int_\Omega r(x,y)\;w(x,y,0)\,\mathrm{d}\,x\,\mathrm{d}\,y \tag{10}$$

and also

$$\Pi_s(r,w) = -\frac{1}{2}\int_\Omega r(x,y)\;w(x,y,0)\,\mathrm{d}\,x\,\mathrm{d}\,y \tag{11}$$

i.e., Π_s equals one half of the work of the external loads. Making use of Eq. (4), Eq. (11) becomes

$$\Pi_s(r) = -\frac{1}{2\,\pi\,E_s} \int_\Omega r(x,y)\,\mathrm{d}\,x\,\mathrm{d}\,y \int_\Omega \frac{r(\xi,\eta)\,\mathrm{d}\,\xi\,\mathrm{d}\,\eta}{d(x,y;\xi,\eta)}. \tag{12}$$

With reference to a rectangular foundation with size length L_1 and L_2, height t_f and equivalent elastic modulus $E_f = E_p/(1-\nu_p^2)$, E_p and ν_p being Young's modulus and Poisson ratio of the isotropic foundation, the parameter characterizing the foundation-soil system is [1]

$$\alpha L_1 = \frac{L_1}{t_f}\sqrt[3]{\frac{12\,E_s\,L_2}{E_f\,L_1}}\,. \tag{13}$$

Values of αL_1 less than 1.4 $(L_2/L_1)^{1/6}$ characterize plates stiffer than substrates, so they perform like rigid foundations, whereas values of αL_1 greater than 150 $(L_2/L_1)^{1/6}$ describe flexible plates. These results also hold for beams in bilateral frictionless contact with an elastic half-space [33].

The surface Ω may be divided into elements of generic shape (triangles, rectangles). In the following, rectangles with length h_{xi} and height h_{yi} are assumed together with piecewise constant base function:

$$\rho_i(x,y) = \begin{cases} 1 & \text{on the } i\text{th element} \\ 0 & \text{elsewhere on } \Omega \end{cases} \tag{14}$$

Hence, vertical displacement and soil reaction for each ith element can be approximated as

$$w^{(i)}(x, y) = \rho_i(x, y)\, q_i, \tag{15}$$

$$r^{(i)}(x, y) = \rho_i(x, y)\, r_i, \tag{16}$$

where q_i and r_i denote nodal vertical displacement and normal traction lumped at the centre of the corresponding ith surface element.

3. FLEXIBLE FOUNDATION: NORMAL TRACTION PRESCRIBED ON THE HALF-SPACE BOUNDARY

For a flexible flat foundation, the normal tractions $r(x, y)$ coincide with the prescribed vertical loads $p(x, y)$ at any point of the surface Ω. Therefore, making use of Eqs. (10) and (9), the potential energy of the substrate with flexible flat foundation Π_{sf} can be written as

$$\Pi_{sf}(w) = U_s(p) - \int_\Omega p(x, y)\, w(x, y, 0)\, \mathrm{d}x\, \mathrm{d}y\,, \tag{17}$$

for prescribed vertical loads $p(x, y)$ on the surface Ω of the half-space.

The prescribed vertical loads $p(x, y)$ can be approximated with the piecewise constant function reported in Eq. (14), thus for each ith element

$$p^{(i)}(x, y) = \rho_i(x, y)\, p_i, \tag{18}$$

where p_i denote the value assigned to the ith surface element. Substituting Eqs. (15) and (18) in the variational principal (17) and assembling over all the elements, the potential energy takes the expression

$$\Pi_{sf}(\mathbf{q}) = \frac{1}{2}\mathbf{p}^{\mathrm{T}}\mathbf{G}\,\mathbf{p} - \mathbf{q}^{\mathrm{T}}\mathbf{H}_f\,\mathbf{p}\,. \tag{19}$$

The components of matrices $\mathbf{H}_f$ and $\mathbf{G}$ are:

$$h_{f,ij} = \int_{y_i}^{y_{i+1}}\int_{x_i}^{x_{i+1}} \rho_i\, \rho_j\, \mathrm{d}x\, \mathrm{d}y \;= \begin{cases} (x_{i+1}-x_i)(y_{i+1}-y_i) = h_{xi}h_{yi} & \text{for } i = j \\ 0 & \text{for } i \neq j \end{cases}, \tag{20}$$

$$g_{ij} = \frac{1}{\pi E_s}\int_{y_i}^{y_{i+1}}\int_{x_i}^{x_{i+1}} \rho_i\, \mathrm{d}x\, \mathrm{d}y \int_{\eta_j}^{\eta_{j+1}}\int_{\xi_j}^{\xi_{j+1}} \frac{\rho_j}{d(x, y; \xi, \eta)}\mathrm{d}\xi\, \mathrm{d}\eta\,, \tag{21}$$

where $(x_i, x_{i+1}; y_i, y_{i+1})$ are the (global) coordinates of the ith surface element and $(\xi_i, \xi_{i+1}; \eta_i, \eta_{i+1})$ are the coordinates of the jth surface element. It is obvious that the square matrix $\mathbf{H}_f$ turns out to be equal to a diagonal matrix, whose elements represent the area of each surface element, whereas the elements of matrix $\mathbf{G}$ are evaluated analytically and are reported in Appendix.

Requiring the total potential energy in Eq. (19) to be stationary, the following system of equations is obtained:

$$\mathbf{H}_f\,\mathbf{q} = \mathbf{G}\,\mathbf{p} \tag{22}$$

that represents the governing equation of the discrete Galerkin method for Eq. (4) when normal tractions p are prescribed on the half-space boundary. The formal solution of Eq. (22) is

$$\mathbf{q} = \mathbf{H}_f^{-1}\,\mathbf{G}\,\mathbf{p}. \tag{23}$$

The average displacement w_{avg} is defined by

$$w_{\text{avg}} = \frac{1}{A}\int_\Omega w(x,y,0)\,\mathrm{d}x\,\mathrm{d}y\,, \tag{24}$$

where A is the area of the surface Ω. Substituting Eq. (4) in Eq. (24) yields

$$w_{\text{avg}} = \frac{1}{\pi E_s A}\int_\Omega \mathrm{d}x\,\mathrm{d}y\int_\Omega \frac{p(\xi,\eta)\,\mathrm{d}\xi\,\mathrm{d}\eta}{d(x,y;\xi,\eta)}\,. \tag{25}$$

Making use of Eq. (18), Eq. (25) reduces to

$$w_{\text{avg}} = \frac{1}{A}\sum_i\sum_j g_{ij}\,p_j\,, \tag{26}$$

Obviously, the same results of Eq. (26) can be obtained starting from Eq. (22):

$$w_{\text{avg}} = \frac{1}{A}\sum_i h_{f,ii}\,q_i = \frac{1}{A}\sum_i\sum_j g_{ij}\,p_j\,. \tag{27}$$

4. RIGID FOUNDATION: VERTICAL DISPLACEMENT PRESCRIBED ON THE HALF-SPACE BOUNDARY

For a rigid flat foundation, the distribution of vertical displacement $w(x, y, 0)$ underlying the footing are prescribed by

$$w(x,y,0) = w_0 + \varphi_{0x}\, y + \varphi_{0y}\, x\,, \tag{28}$$

where w_0, φ_{0x}, and φ_{0y} are specified at the origin $x = y = z = 0$ (Fig. 1).

Making use of Eq. (12), the potential energy of the rigid foundation-substrate system Π_{sr} can be written as:

$$\Pi_{sr}(r,w) = \Pi_s(r,w) - \int_\Omega [p(x,y) - r(x,y)]\, w(x,y,0)\, \mathrm{d}\,x\, \mathrm{d}\,y\,. \tag{29}$$

Substituting Eq. (28) in Eq. (29) yields

$$\Pi_{sr}(r,\mathbf{q}_0) = -U_s(r) - \left\{ w_0\left[P - \int_\Omega r\, \mathrm{d}\Omega\right] + \varphi_{0x}\left[M_x - \int_\Omega r\, y\, \mathrm{d}\Omega\right] + \varphi_{0y}\left[M_y - \int_\Omega r\, x\, \mathrm{d}\Omega\right]\right\} \tag{30}$$

where the vector $\mathbf{q}_0 = [w_0, \varphi_{0x}, \varphi_{0y}]^{\mathrm{T}}$ collects the displacements prescribed at the origin and

$$P = \int_\Omega p\, \mathrm{d}\,x, \qquad M_x = \int_\Omega p\, y\, \mathrm{d}\Omega, \qquad M_y = \int_\Omega p\, x\, \mathrm{d}\Omega \tag{31}$$

are the three external load resultants. It can readily be noted that, in Eq. (30), each difference in square brackets corresponds to a global equilibrium equation.

Substituting Eqs. (15) and (16) into the variational principle (30) and assembling over all substrate elements

$$\Pi_{sr}(\mathbf{r},\mathbf{q}_0) = \mathbf{q}_0^{\mathrm{T}}\mathbf{H}_r\, \mathbf{r} - \mathbf{q}_0^{\mathrm{T}}\mathbf{f} - \frac{1}{2}\mathbf{r}^{\mathrm{T}}\mathbf{G}\,\mathbf{r}\,, \tag{32}$$

where the elements of matrix $\mathbf{G}$ are reported in Appendix, the vector $\mathbf{f} = [P, M_x, M_y]^{\mathrm{T}}$ collects the three external load and

$$\mathbf{H}_r = \begin{bmatrix} \mathbf{h}_{r0}^{\mathrm{T}} \\ \mathbf{h}_{rx}^{\mathrm{T}} \\ \mathbf{h}_{ry}^{\mathrm{T}} \end{bmatrix}, \tag{33}$$

where

$$h_{r0,i} = \int_{y_i}^{y_{i+1}} \int_{x_i}^{x_{i+1}} \rho_i\, \mathrm{d}\,x\, \mathrm{d}\,y = h_{xi} h_{yi}\,, \tag{34}$$

$$h_{rx,i} = \int_{y_i}^{y_{i+1}} \int_{x_i}^{x_{i+1}} \rho_i\, x\, \mathrm{d}\,x\, \mathrm{d}\,y = h_{xi}\, h_{yi}\, (x_i + x_{i+1})/2\,. \tag{35}$$

$$h_{ry,i} = \int_{y_i}^{y_{i+1}} \int_{x_i}^{x_{i+1}} \rho_i \; y \, \mathrm{d}\,x \, \mathrm{d}\,y = h_{xi} \, h_{yi} \, (y_i + y_{i+1})/2 \tag{36}$$

represent the area and first moment of area with respect to x-axis or y-axis of each surface element, respectively. Obviously, the diagonal of the matrix $\mathbf{H}_f$, whose components are reported in Eq. (20), coincides with $\mathbf{h}_{r0}$.

Requiring the potential energy in Eq. (32) to be stationary, the following system of equations is obtained

$$\begin{bmatrix} \mathbf{0} & \mathbf{H}_r \\ \mathbf{H}_r^{\mathrm{T}} & -\mathbf{G} \end{bmatrix} \begin{Bmatrix} \mathbf{q}_0 \\ \mathbf{r} \end{Bmatrix} = \begin{Bmatrix} \mathbf{f} \\ \mathbf{0} \end{Bmatrix} \tag{37}$$

The first relation of Eq. (37), $\mathbf{H}_r \, \mathbf{r} = \mathbf{f}$, imposes global equilibrium equation between the substrate tractions $\mathbf{r}$ and the external load resultants $\mathbf{f}$, whereas the second relation

$$\mathbf{G} \, \mathbf{r} = \mathbf{H}_r^{\mathrm{T}} \, \mathbf{q}_0, \tag{38}$$

represents the governing equation of the discrete Galerkin method for Eq. (4) with displacements prescribed by Eq. (28). It is worth remarking that Eq. (4) represent a weakly singular integral equation of the first kind with prescribed function $w(x, y, 0)$. Existence, uniqueness and regularity results for the unknown $r(x, y, 0)$ are reported in [44]. Stability and convergence properties of Galerkin approximations given by Eq. (38) was proved in [29] for both piecewise constant and piecewise-linear boundary elements. Once normal tractions on boundary half-space are found, displacements and stresses at arbitrary points of the half-space can be evaluated analytically adopting the procedures described in [10, 12].

The formal solutions to Eq. (37) yields

$$\mathbf{r} = \mathbf{G}^{-1} \, \mathbf{H}_r^{\mathrm{T}} \, \mathbf{q}_0 = \mathbf{G}^{-1} \, (w_0 \, \mathbf{h}_{r0} + \varphi_{0x} \, \mathbf{h}_{rx} + \varphi_{0y} \, \mathbf{h}_{ry}), \tag{39}$$

$$\mathbf{K}_r \, \mathbf{q}_0 = \mathbf{f}, \tag{40}$$

where the stiffness matrix of the rigid foundation-substrate system

$$\mathbf{K}_r = \mathbf{H}_r \, \mathbf{G}^{-1} \, \mathbf{H}_r^{\mathrm{T}} \tag{41}$$

is a 3-by-3 matrix.

4.1 Static stiffnesses for rigid foundation

The first row of Eq. (40) reads as

$$w_0 + k_{r,12}/k_{r,11}\ \varphi_{0x} + k_{r,12}/k_{r,11}\ \varphi_{0y} = P/k_{r,11}, \tag{42}$$

hence, introducing the center of stiffness K having coordinates

$$x_K = k_{r,12}/k_{r,11}, \qquad y_K = k_{r,13}/k_{r,11}, \tag{43}$$

the left hand-side of Eq. (42) represents the vertical displacement w_K in correspondence of the center of stiffness and $k_{r,11}$ stands for the vertical stiffness k_V of the rigid foundation.

Making use of Eqs. (42) and (43), the second and third rows of Eq. (40) reduces to

$$k_{\varphi,11}\ \varphi_{0x} + k_{\varphi,12}\ \varphi_{0y} = M_x - P\ x_K, \tag{44}$$

$$k_{\varphi,12}\ \varphi_{0x} + k_{\varphi,22}\ \varphi_{0y} = M_y - P\ y_K, \tag{45}$$

where

$$k_{\varphi,11} = k_{r,22} - k_{r,12}\ x_K, \tag{46a}$$

$$k_{\varphi,12} = k_{r,23} - k_{r,12}\ k_{r,13}/k_{r,11}, \tag{46b}$$

$$k_{\varphi,22} = k_{r,33} - k_{r,13}\ y_K. \tag{46c}$$

The rotational stiffness coefficients of the rigid foundation coincide with the eigenvalues of the system of equations (44) and (45) and the corresponding eigenvectors identify the direction of the principal axes of stiffness. In particular, the two principal rotational stiffness $k_{\varphi,\mathrm{I}}$ and $k_{\varphi,\mathrm{II}}$ are

$$k_{\varphi,\mathrm{I}}, k_{\varphi,\mathrm{II}} = \frac{1}{2}\left[k_{\varphi,11} + k_{\varphi,22} \pm \sqrt{\left(k_{\varphi,11} - k_{\varphi,22}\right)^2 + 4k_{\varphi,12}^2}\right] \tag{47}$$

and the angle α between the principal axis of stiffness and the x-axis is given by

$$\tan 2\alpha = \frac{k_{\varphi,12}}{k_{\varphi,11} - k_{\varphi,22}}. \tag{48}$$

It is worth remark that Eqs. (43) and (48) are mesh-dependent, hence the center of stiffness K and the angle α may not coincide with the corresponding geometric center of area and angle between the principal axis and the x-axis of the foundation shape. This means that a concentrated vertical force P has to be applied at the center of stiffness K in case of a rigid indenter with an unsymmetrical shape, in order to have no rotation of the indenter with respect to x and/or y axis. This aspect was pointed out by Conway and Farnham [20] by performing numerical tests on unsymmetrical L-shaped punches. Nonetheless, for a foundation with both double symmetric shape and mesh, direct computations show that the center of stiffness K and the principal axes of stiffness coincide with the geometric centroid and the geometric principal axes, respectively.

Finally, the rotations and moments referred the principal axes of stiffness transform as usual

$$\varphi_{\mathrm{I}} = \varphi_{0x} \cos\alpha + \varphi_{0y} \sin\alpha, \tag{49a}$$

$$\varphi_{\mathrm{II}} = -\varphi_{0x} \sin\alpha + \varphi_{0y} \cos\alpha. \tag{49b}$$

$$\varphi_{0x} = \varphi_{\mathrm{I}} \cos\alpha - \varphi_{\mathrm{II}} \sin\alpha, \tag{50a}$$

$$\varphi_{0y} = \varphi_{\mathrm{I}} \sin\alpha + \varphi_{\mathrm{II}} \cos\alpha. \tag{50b}$$

$$M_{\mathrm{I}} = (M_x - P\, x_K) \cos\alpha + (M_y - P\, y_K) \sin\alpha, \tag{51a}$$

$$M_{\mathrm{II}} = -(M_x - P\, x_K) \sin\alpha + (M_y - P\, y_K) \cos\alpha. \tag{51b}$$

The resolving Eqs. (39) and (40) reduce to:

$$\mathbf{r} = w_K\, \mathbf{G}^{-1}\, \mathbf{h}_{r0} + \varphi_{0x}\, \mathbf{G}^{-1}\, (\mathbf{h}_{rx} - x_K\, \mathbf{h}_{r0}) + \varphi_{0y}\, \mathbf{G}^{-1}\, (\mathbf{h}_{ry} - y_K\, \mathbf{h}_{r0}), \tag{52}$$

$$w_K = P/k_v, \quad \varphi_{\mathrm{I}} = M_{\mathrm{I}}/k_{\varphi,\mathrm{I}}, \quad \varphi_{\mathrm{II}} = M_{\mathrm{II}}/k_{\varphi,\mathrm{II}}. \tag{53}$$

5. SURFACE DISCRETIZATION

The surface Ω of the footing is subdivided into quadrilateral elements and the simplest subdivision is obviously a regular mesh. However, it is well known that the solution of Eq. (4) with prescribed displacements exhibits singular behaviour near the edges and corners [45]. Therefore, a regular mesh may not be able to describe correctly surface displacements and substrate reaction at edges and corners of the indenter. In order to obtain accurate results, it is common to use power graded meshes [30, 46, 47], Alternatively, edge and corner singularities can be treated using singular boundary elements close to edges and corners, see [48, 49] and references cited therein.

Power graded meshes are characterized by a grading exponent β ≥ 1. A generic dimensionless coordinate t, on the interval (0,1) is described by the following expression:

$$t_j = \begin{cases} \dfrac{1}{2}\left[\left(\dfrac{2j}{n}\right)^{\beta} - 1\right] & \text{for } 0 \le j \le n/2 \\ -t_{n-j} & \text{for } n/2 < j \le n \end{cases} \tag{54}$$

where n is the number of points on the interval. For β = 1 the mesh turns out to be uniform, but as β increases, the points are more concentrated at the end of the interval. In the following, a square with unitary side length is considered and the same number of subdivisions is adopted along x and y axes ($n_x = n_y = n$).

Considering the squares in Fig. 2, it is worth noting that for increasing β, the elements near surface edges and corners tend to be smaller and smaller, however, elements close to the origin tend to be bigger. Consequently, the exponent β in Eq. (54) has to be chosen in order to obtain accurate results both near surface edges and close to the origin.

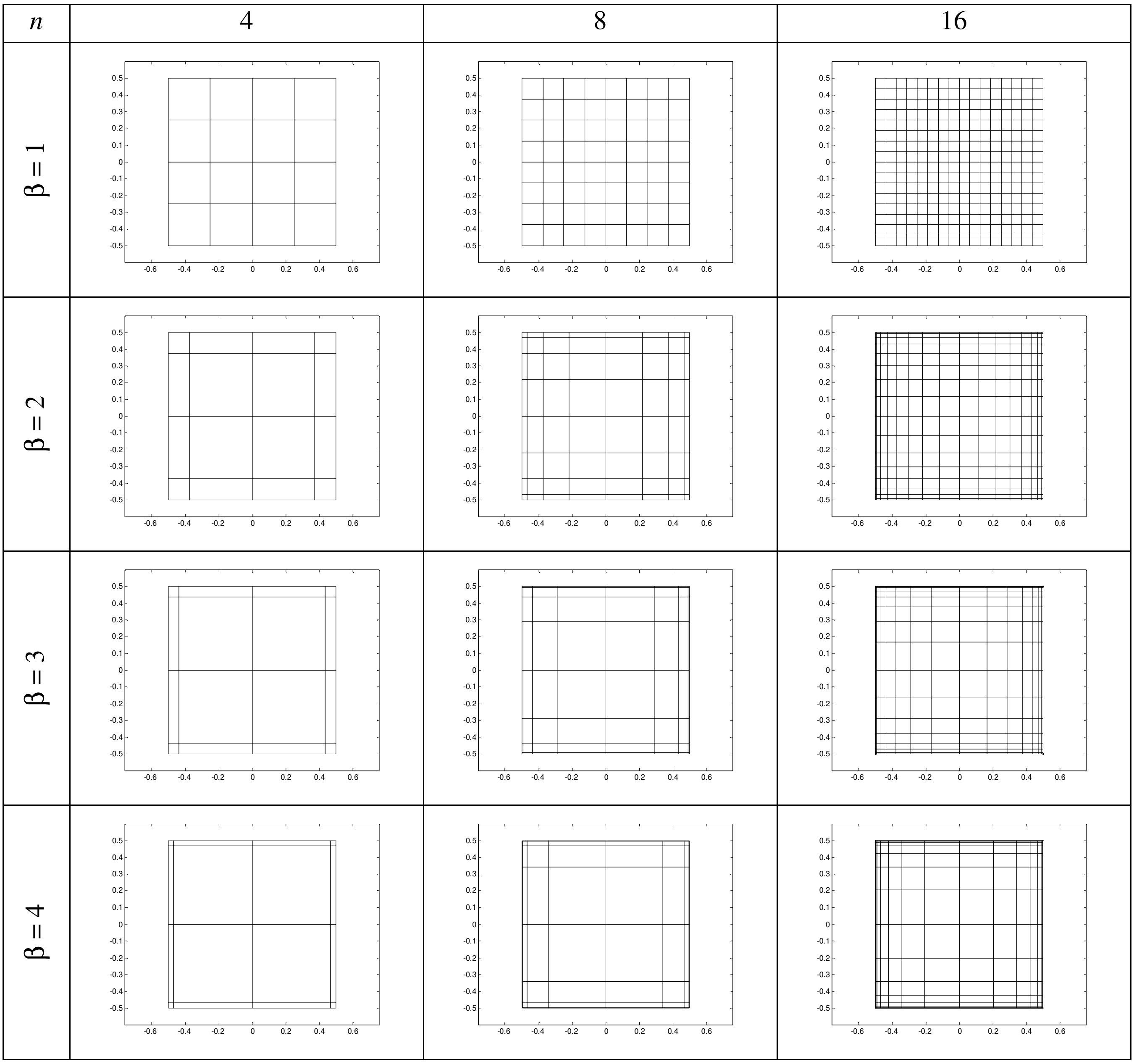

Fig. 2. Examples of power-graded meshes for a square with unitary side length varying the number of element n and grading exponent β.

6. UNIFORM PRESSURE APPLIED TO A RECTANGULAR SURFACE

In order to ascertain the correctness of Eq. (23) and of the components of the flexibility matrix $\mathbf{G}$ of the half-space, a uniform pressure p applied to a generic rectangular surface having length L_1 and width L_2 (Fig. 3) is considered. In this case, the analytic solution was determined by Love [9, 15, 17].

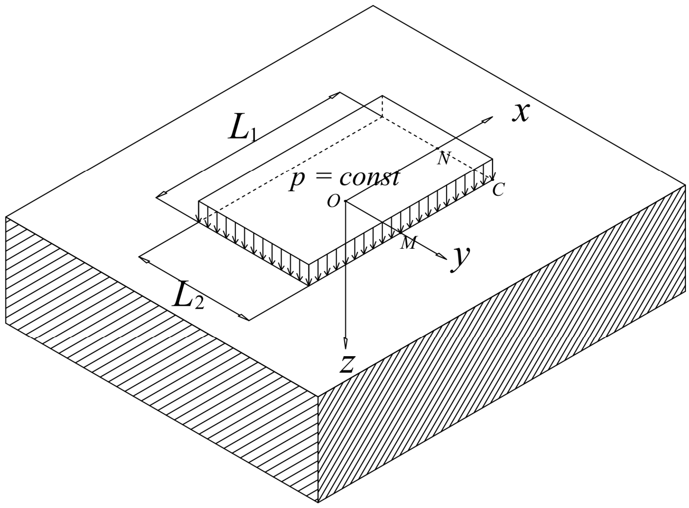

Fig. 3. Elastic half-space loaded by a constant pressure p over a rectangular surface.

Dimensionless displacements are evaluated at four points O, N, M, C (Fig. 3) varying exponent β and increasing the number of subdivisions along each side. The first point O coincides with the origin of the coordinate system; the second one, M, is at the midpoint of the edge parallel to x-axis; the third one, N, is at the midpoint of the edge parallel to y-axis; and the last one, C, is corner of the loaded rectangle surface. It is worth noting that the adopted surface discretizations do not allow to evaluate displacements at the exact points described above since each displacement value is applied in the centre of the corresponding boundary element.

The case of a square loaded surface ($L_1 = L_2 = L$) having the same number of elements in x and y directions ($n_x = n_y = n$) is considered first. Obviously, the displacements at points M and N are equal. The analytic values w_a determined by Love [9, 15, 17] are

$$w_O = w_a(0, 0) = 1.122\, pL_1/E_s, \tag{55a}$$

$$w_M = w_N = w_a(0, L_1/2) = 0.7659\, pL_1/E_s, \tag{55b}$$

$$w_C = w_a(L_1/2, L_1/2) = 0.5611\, pL_1/E_s. \tag{55c}$$

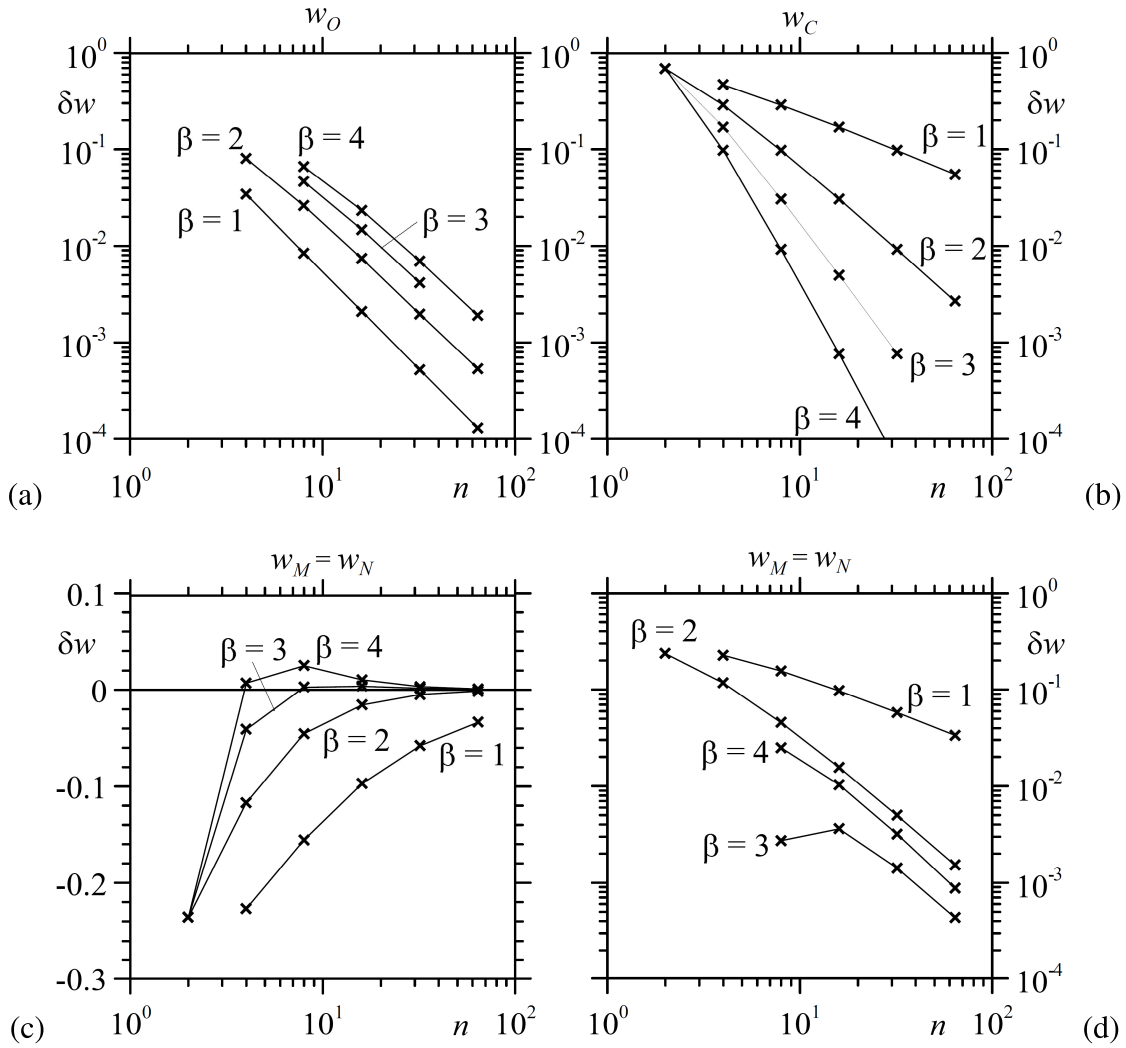

Fig. 4. Relative errors δw for displacements evaluated at points (a) O, (b) C and (c, d) M, N.

Fig. 4 show the relative error $\delta w = (w - w_a)/w_a$ for the three displacements reported in Eqs. (55). In particular, Fig. 4a shows the relative errors for the displacement at origin. In this case, the convergence ratios are coincident and close to n^{-2} for all surface discretization cases. However, relative errors are small also for the uniform discretization case. Indeed, for n = 32 and β = 1, relative error is close to 0.5%, whereas for n = 16 and β = 3, relative error is close to 4%. Considering the displacement at corner (Fig. 4b), the convergence ratios are small for β = 1 and 2 ($n^{-0.75}$ and $n^{-1.7}$, respectively), whereas for β = 3 and 4 convergence ratios are close to $n^{-2.7}$ and $n^{-3.7}$, respectively. For n = 32 and β = 1, relative error is close to 10%, whereas for n = 16 and β = 3, relative error is close to 0.8%. Finally, Figs. 4c and 4d show relative errors related to the displacement at edge midpoint M or N. In this case, errors for β equal to 3 and 4 do not have a monotonic behaviour. Nonetheless, neglecting values for $n = 4$, errors can still be represented in bi-logarithmic scale. Convergence ratio for $\beta = 1$ is close to $n^{-0.75}$, whereas for β equal to 2, 3 and 4 ratios are almost coincident and close to n^{-1}. For $\beta = 3$ errors are lower with respect to other discretization cases, Therefore, for this example the power graded mesh with $\beta = 3$ turns out to be quite effective.

Figs. 5a and 5b show the dimensionless displacement $w^* = w/[pL_1/E_s]$ along the x-axis and along the diagonal of the square surface, where the coordinate is equal to $\sqrt{2}\,x$, for increasing β and assuming $n = 16$. In this example the exponent β does not influence results significantly.

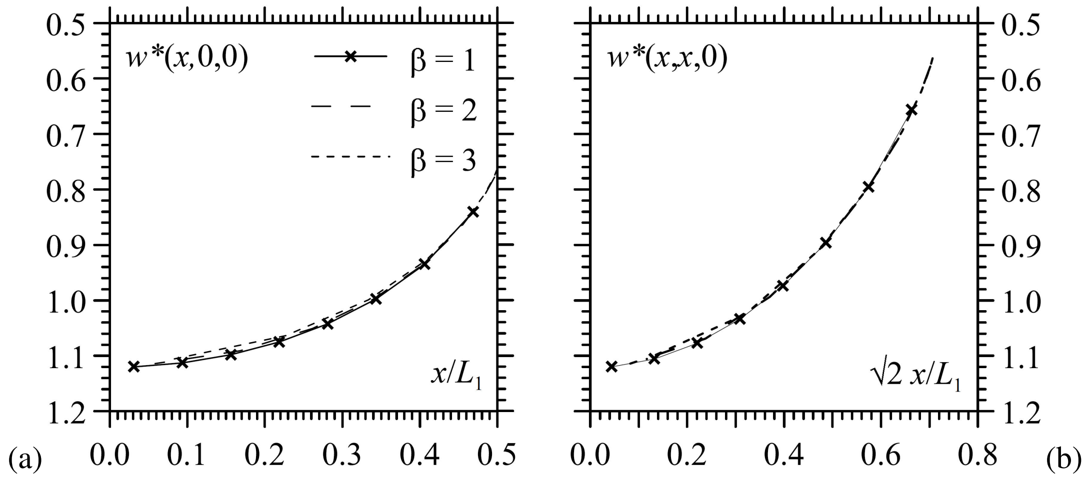

Fig. 5. Dimensionless vertical displacements w^* (a) along the x-axis and (b) along the diagonal due to a uniform pressure over a square surface.

With reference to rectangular surfaces loaded by uniform pressure, Fig. 6 shows dimensionless vertical displacements w^* at points O, M, N and C versus the ratio L_1/L_2. The surface discretization is characterized by a power graded mesh with $\beta = 3$ and assuming $n_x = n_y = 64$. Results are in good agreement with Love's solution [9, 15, 17].

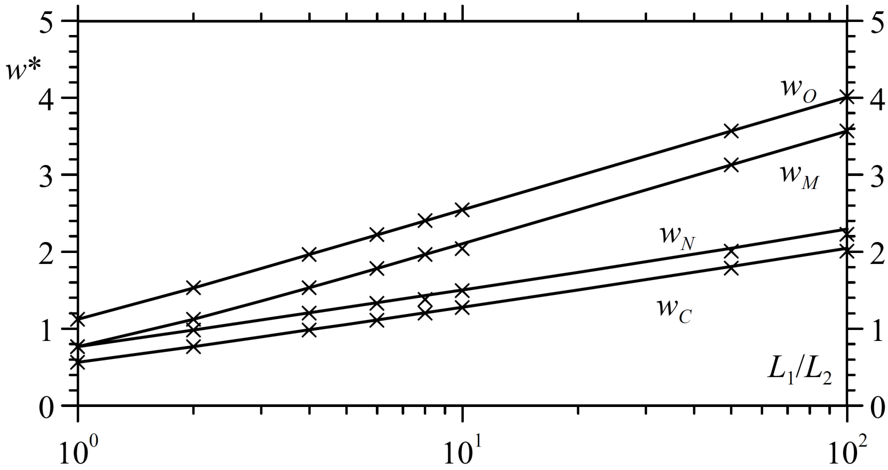

Fig. 6. Dimensionless vertical displacements w^* beneath a rectangular area due to a uniform pressure (continuous lines for present analysis, cross symbols for Love's solution).

Making use of Eq. (25), the average displacement w_{avg} for an uniform vertical pressure distribution over a rectangle having total load resultant $P = p\, L_1\, L_2$ reduces to

$$w_{\mathrm{avg}} = \frac{P}{(L_1\, L_2)^2}\, g_{ii}(L_1, L_2)\,, \tag{56}$$

where $g_{ii}(L_1, L_2)$ is reported in Appendix and must be evaluated replacing l_{xi} and l_{yi} with L_1 and L_2, respectively, and gives an analytical estimates for w_{avg}, whereas numerical results are derived by using Eq. (27).

Usually, the average displacement w_{avg} is written in the form [50]:

$$w_{\mathrm{avg}} = \frac{P}{c_{vf}\, E_s \sqrt{L_1 L_2}} \tag{57}$$

where c_{vf} is reported in Table 1 for some values of the L_1/L_2 ratio. Therefore, the vertical stiffness k_{vf} of a flexible foundation is

$$k_{vf} = \frac{P}{w_{\mathrm{avg}}} = c_{vf}\, E_s \sqrt{L_1 L_2}\ . \tag{58}$$

Tab. 1. Dimensionless vertical stiffness c_{vf} for flexible rectangular foundation.

L_1/L_2	1	1.5	2	3	5	10	100
Analytical integration Eq. (56) Present analysis (β=3, n_x=n_y=64)	1.057	1.067	1.088	1.134	1.225	1.408	2.708
Timoshenko and Goodier 1951 [50]	1.05	1.06	1.09	1.14	1.22	1.41	2.70

7. RIGID RECTANGULAR FOUNDATION

In this section a rigid rectangular foundation with size length L_1 and L_2 is considered, its centroid is located at the origin and the x and y axes coincide with the centroidal axes of the foundation (Fig. 1). Vertical load P and moments M_x, M_y are applied at the origin.

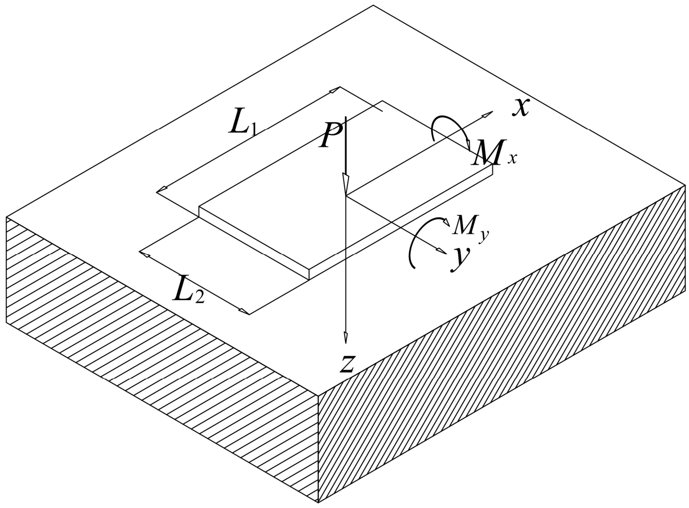

Fig. 7. Rigid rectangular foundation resting on an elastic half-space.

The resolving Eqs. (51) and (52) reduce to:

$$\mathbf{r} = w_0\, \mathbf{G}^{-1}\, \mathbf{h}_{r0} + \varphi_{0x}\, \mathbf{G}^{-1}\, \mathbf{h}_{rx} + \varphi_{0y}\, \mathbf{G}^{-1}\, \mathbf{h}_{ry}, \tag{59}$$

$$w_0 = P/k_v, \quad \varphi_{0x} = M_x/k_{\varphi x}, \quad \varphi_{0y} = M_x/k_{\varphi y}, \tag{60}$$

where the vertical stiffness k_v and the rotational stiffnesses $k_{\varphi x}$, $k_{\varphi y}$ can be written as

$$k_v = \mathbf{h}_{r0}^{\mathrm{T}}\, \mathbf{G}^{-1}\, \mathbf{h}_{r0}, \tag{61a}$$

$$k_{\varphi x} = \mathbf{h}_{rx}^{\mathrm{T}}\, \mathbf{G}^{-1}\, \mathbf{h}_{rx}, \tag{61b}$$

$$k_{\varphi y} = \mathbf{h}_{ry}^{\mathrm{T}}\, \mathbf{G}^{-1}\, \mathbf{h}_{ry}, \tag{61c}$$

7.1 Rigid square foundation with vertical load

The case of a square foundation ($L_1 = L_2 = L$) having the same number of elements in x and y directions ($n_x = n_y = n$) is considered first. Taking into account the vertical load P only, adopting n = 16 elements for each side and varying β, Fig. 8a shows dimensionless normal traction $r(x, 0)/(P/L^2)$ along x-axis, whereas Figs. 8c shows dimensionless normal traction $r(x, x)/(P/L^2)$ along the diagonal. The singularities of normal tractions close to contact surface edge and corner are highlighted in Fig. 8b and d, respectively, by adopting n = 64 elements for each side. It is worth noting that the estimates of the exponent of the edge and corner singularity are equal to 0.5 and 0.7, respectively, in good agreement with the estimates reported in [51, 52, 53]. In Fig. 9, dimensionless normal tractions are shown by adopting a three-dimensional representation. It is clear that normal tractions assume quite constant value close to the origin, whereas they increase rapidly in proximity of edges and corners. Results obtained with the uniform mesh are not able to represent correctly the behaviour at surface edges and corners, whereas increasing β, the values near edges and corners increase rapidly.

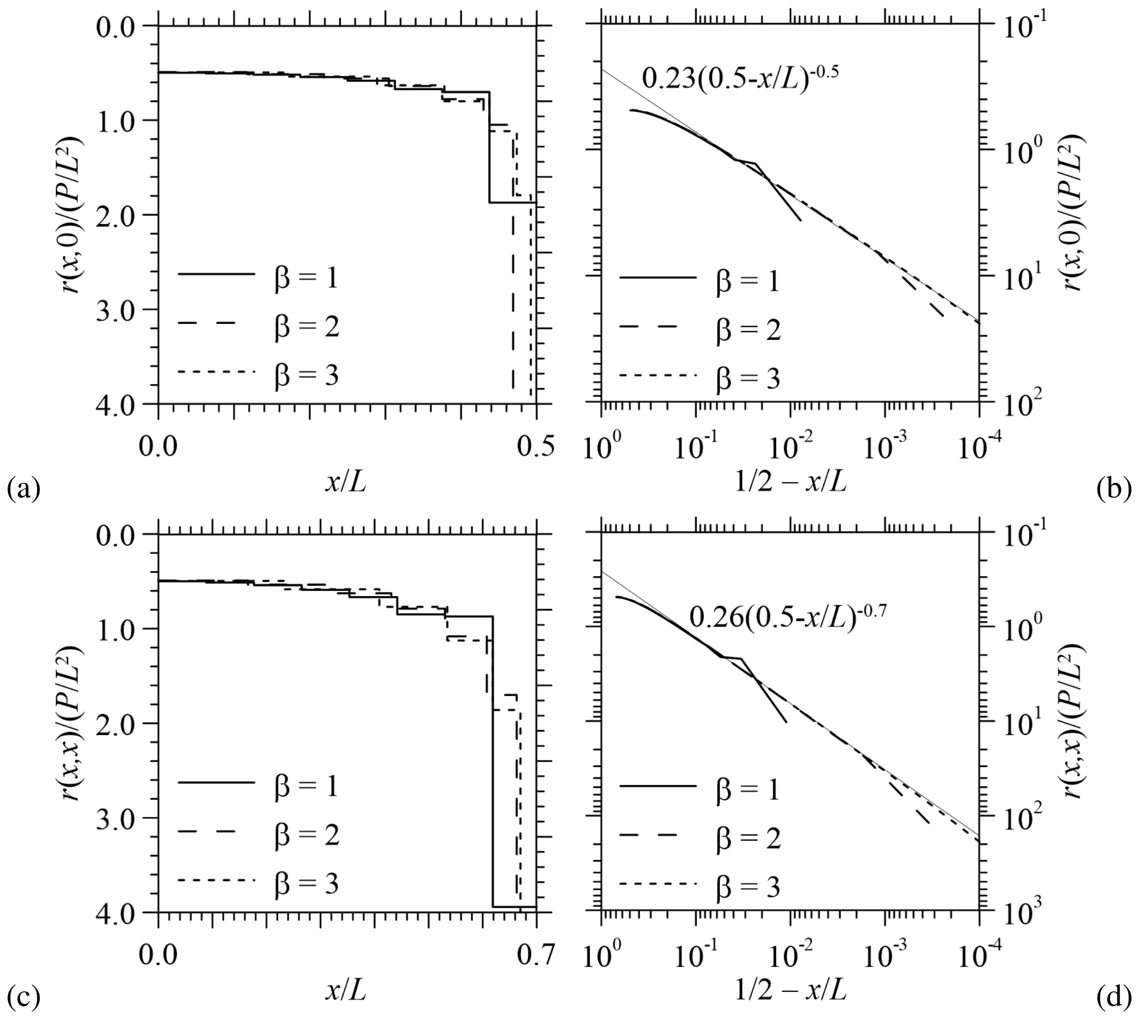

Fig. 8. Dimensionless normal traction due to a vertical force (a) along x-axis, (b) at the midpoint of the edge parallel to y-axis, (c) along the diagonal and (d) at the corner.

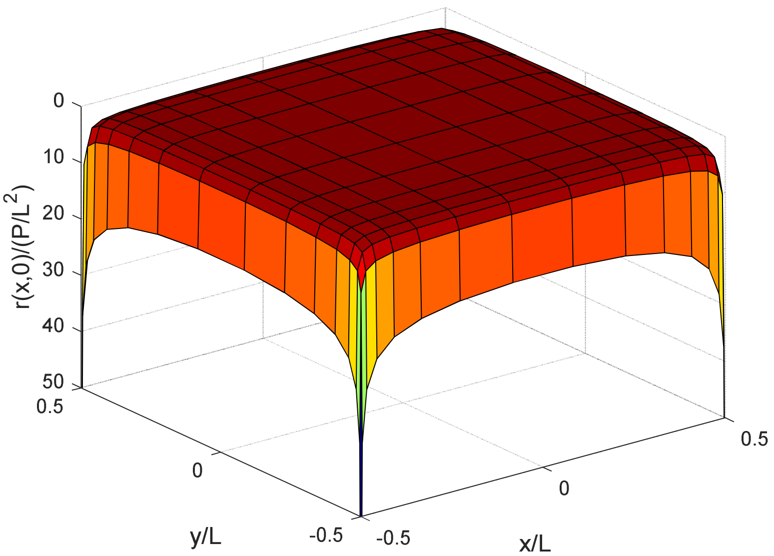

Fig. 9. Dimensionless normal traction due to a vertical force. Square surface is subdivided with a power graded mesh having 16 elements for each side and β = 3.

Applying Rayleigh considerations [54], it is worth noting that the vertical stiffness k_v of a rigid square foundation may be delimited by an upper and lower bound:

$$1.1284 = \frac{2}{\sqrt{\pi}} < \frac{k_v}{E_s\ L} < \sqrt{2} = 1.4142\,, \tag{62}$$

where the lower bound represents the stiffness of a circle having the same area of the square and the upper bound is the stiffness of the circle circumscribed to the square area, see also [1] for bounds on rectangular plates.

The vertical stiffness for the rigid square foundation obtained with $\beta = 4$ and $n = 2^7$ is considered as reference solution:

$$k_v^{REF} = 1.1523\ E_s L \tag{63}$$

Table 2 shows values of k_v obtained by different researchers and by adopting various methods of solution. The vertical stiffness obtained with the present model is close to the results proposed by [24, 29, 48], In particular, Dempsey and Li [24] used numerical integration with Gauss quadrature adopting a graded discretization of the surface, whereas [29] made use of GBEM with graded mesh and [48, 49] adopted BEM with singular elements.

Tab. 2. Dimensionless vertical stiffness values for rigid square foundation.

Author	Method	$k_v/(E_s L)$
Present analysis	GBEM with graded mesh	1.1523
Eskandari-Ghadi et al. 2017 [49]	BEM with singular elements	1.152
Guzina et al. 2006 [48]	BEM with singular elements	1.152
Bosakov 2003 [25]	Orthogonal polynomials	1.146
Erwin et al. 1990 [29]	GBEM with graded mesh	1.1523
Dempsey and Li 1989 [24]	BEM with graded mesh	1.1523
Pais and Kausel 1988 [28]	Review existing solutions	1.175
Conway and Farnham 1968 [20]	BEM with uniform mesh	1.114
Whitman and Richart 1967 [27]	-	1.080
Gorbunov and Posadov 1961 [1]	Power series	1.095

The errors $\delta k_v = (k_v^{REF} - k_v)/k_v^{REF}$ are evaluated varying β and increasing the number of subdivisions along each side of the surface. Relative errors are shown in Figs. 10a and 10b varying n and $n_{TOT} = n^2$, respectively.

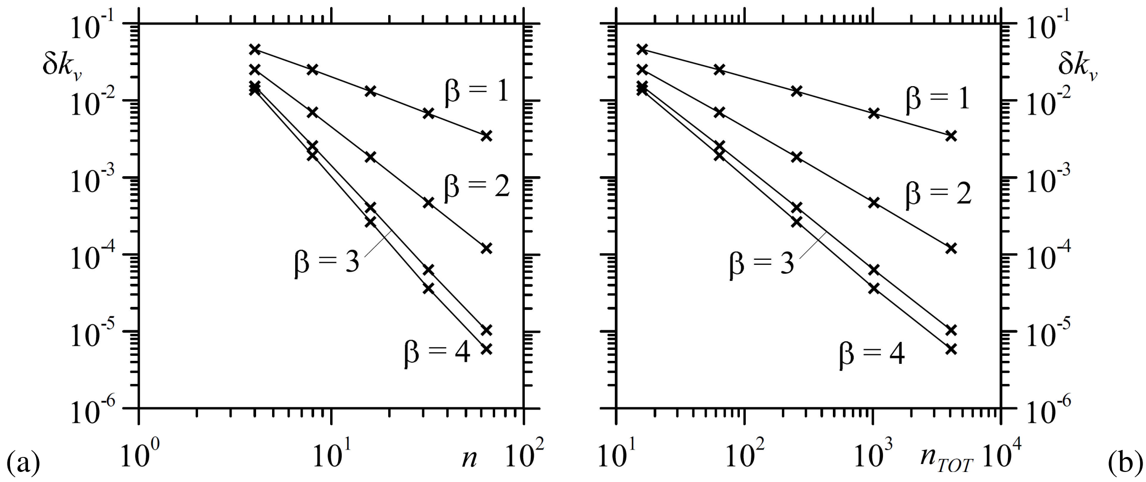

Fig. 10. Relative errors for k_v varying (a) the number of subdivisions along each surface side and (b) the total number of boundary elements.

Fig. 10b clearly shows that vertical stiffness converge with different converge rates varying β. In particular, the results obtained with the uniform mesh converge to the reference solution with rates close to n^{-1} and $n_{TOT}^{-0.5}$, whereas rates are close to n^{-2} and $n_{TOT}^{-1.0}$ for β equal to 2. Convergence rates obtained with β equal to 3 ($n^{-2.7}$ and $n_{TOT}^{-1.35}$) turn out to be quite close to those obtained with β equal to 4. Moreover, for β = 3 and $n = 2^6$, relative error is less than 10^{-4} (10^{-2} %). Considering convergence tests shown in Figs. 10a and 10b, the soil surface discretization obtained with β = 3 can be considered the most effective with respect to other cases. In particular, the case β = 4 does not increase significantly the results accuracy, but generates larger boundary elements close to the origin of the surface.

7.2 Rotational stiffness for a rigid square foundation with applied moment M_x

For a rigid foundation with applied moment M_x, the rotational stiffness can be derived by Eq. (61b). Considering a square foundation ($L_1 = L_2 = L$) with the same number of elements in x and y directions ($n_x = n_y = n$), the rotational stiffness obtained adopting β = 4 and $n_x = n_y = 2^7$ is considered as the reference solution:

$$k_{\varphi x}^{REF} = 0.2601\, E_s L^3, \tag{64}$$

This estimates is close to the results proposed in [27].

The errors $\delta k_{\varphi x} = (k_{\varphi x}^{REF} - k_{\varphi x}) / k_{\varphi x}^{REF}$ are evaluated varying β and increasing the number of subdivisions along each side of the surface. Relative errors are shown in Fig. 11a and 11b varying n and $n_{\mathrm{TOT}} = n^2$, respectively. Fig. 11b clearly shows that rotational stiffness converge with different rates varying β, In particular, the results obtained with the uniform mesh converge to the reference solution with rates close to n^{-1} and $n_{TOT}^{-0.5}$ for β equal to 1, whereas rates are close to n^{-2} and n_{TOT}^{-1}, for β equal to 2. Convergence ratios obtained with β equal to 3 ($n^{-2.8}$ and $n_{TOT}^{-1.4}$,) turn out to be coincident with the one obtained with β equal to 4. Moreover, for β = 3 and $n_x = n_x = 2^6$, relative error is less than $5{\times}10^{-5}$. Therefore, in this case, similarly to the previous example, the power graded mesh with β = 3 represents the best choice for the surface discretization.

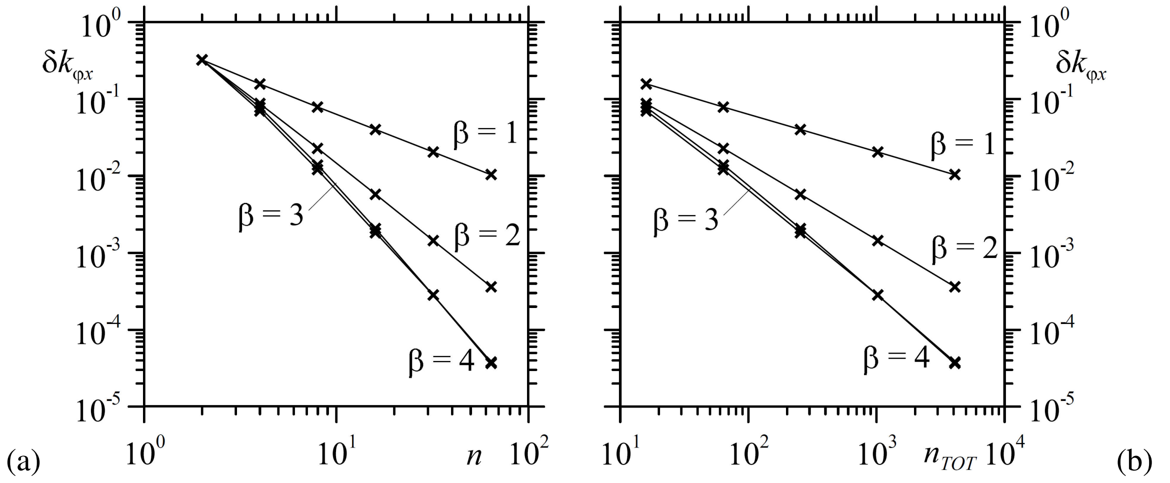

Fig. 11. Relative errors for $k_{\varphi x}$ varying (a) the number of subdivisions along each surface side and (b) the total number of boundary elements.

7.3 Stiffnesses of rigid rectangular foundation

Adopting a power graded mesh having $\beta = 3$ and $n_x = n_y = 2^6$, the dimensionless vertical stiffness $c_{vr} = k_v / \left(E_s \sqrt{L_1 L_2} \right)$ and rotational stiffness $c_{\varphi x} = k_{\varphi x} / \left(E_s L_1 L_2^2 \right)$ are shown with continuous lines in Fig. 12 versus L_1/L_2 ratio, where cross symbols represent data reported in [27]. Therefore, the present model turns out to be effective also for rigid rectangular foundations and the power graded mesh with $\beta = 3$ is sufficient to obtain accurate values.

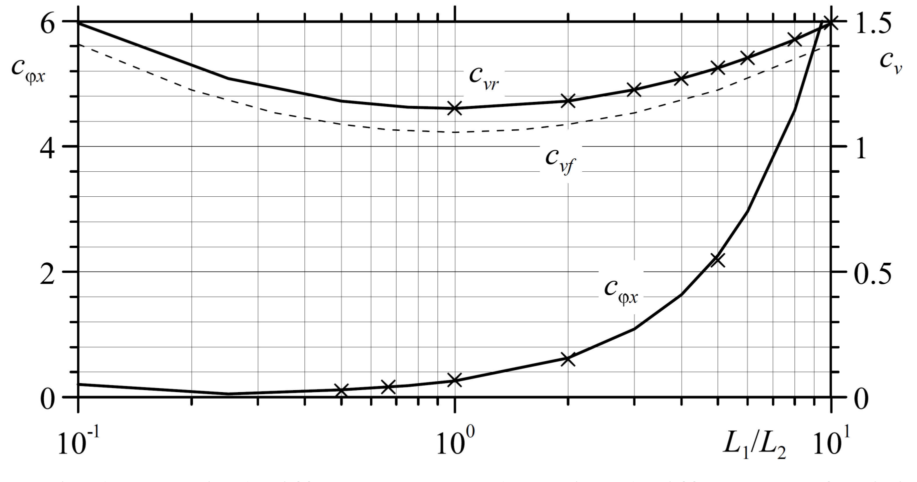

Fig. 12. Dimensionless vertical stiffness c_{vf}, c_{vr} and rotational stiffness $c_{\varphi x}$ of a rigid rectangular foundation varying L_1/L_2 ratio. (continuous lines for present analysis, cross symbol for Whitman and Richart (1967) data).

8. L-SHAPED RIGID FOUNDATIONS

In this section, three type of L-shaped rigid foundations are considered (Fig. 13). In particular, a symmetrical L-shaped rigid foundation is reported in Fig. 13a and was analysed by Erwin and Stephan [30]. The contact surface is formed from a square of side length 2*L* out of which a corner square of side length *L* was removed. The two unsymmetrical cases reported in Figs. 13b and 13c were considered by Conway and Farnham [20].

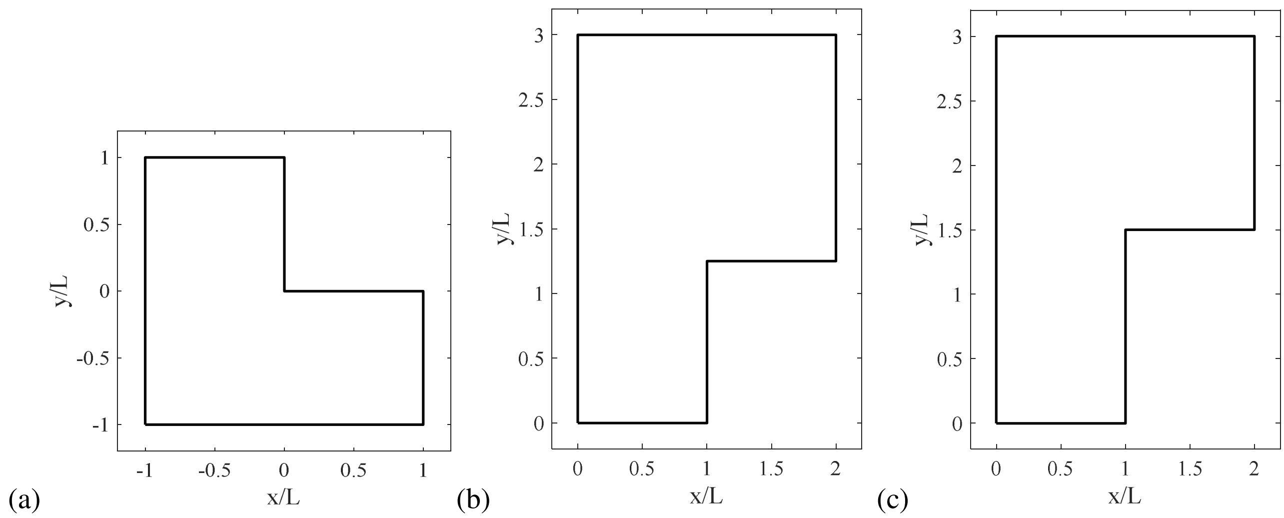

Fig. 13. L-shaped rigid foundations proposed by (a) Erwin and Stephan [30], (b) Conway and Farnham #1 [20] and (c) Conway and Farnham #2 [20].

8.1 Stiffness parameters of L-shaped rigid foundations

Translational and rotational stiffness parameters of the rigid footing are evaluated with the proposed numerical model, together with the position of the centre of stiffness *K* with respect to the geometric centre of area *C*, and the orientation of the principal axis of stiffness with respect to the principal axis of inertia. Particular attention is also given to the contact surface discretization and several convergence tests are performed. For this purpose, on one hand, a refined contact surface discretization characterized by the same power-graded mesh with $\beta = 3$ for each quadrilateral portion of the L-shaped punch is adopted (Fig. 14a), in order to work with a model with smaller surface FEs both close to the external edges and close to the inner corner of the punch. On the other hand, a simpler power-graded mesh with $\beta = 3$ characterized by small surface FEs only close to the external edges of the punch is considered (Fig. 14b). Furthermore, the simplest case of a regular contact surface discretization, namely a power graded mesh with β = 1, is adopted (Fig. 14c).

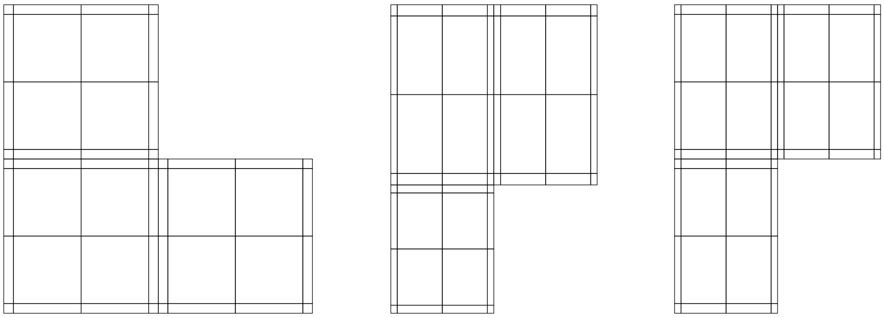

a

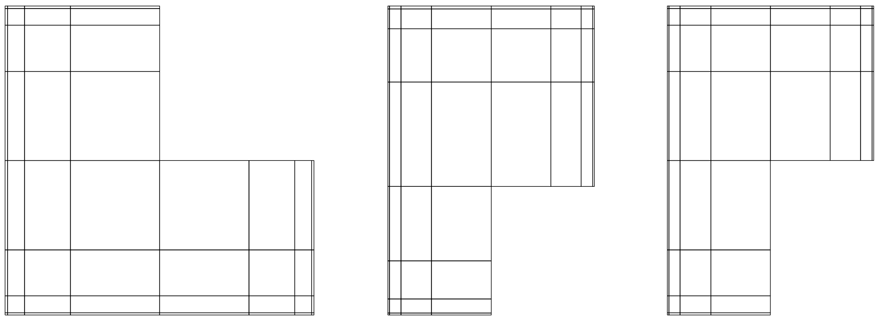

b

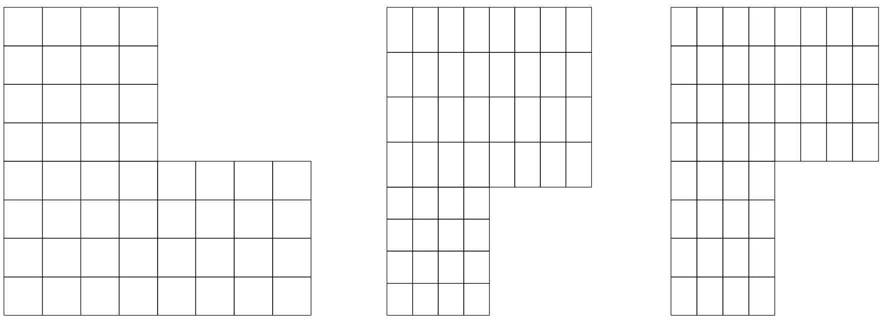

c

Fig. 14. L-shaped rigid foundations having 8 subdivisions along x and y directions, and with (a) refined power-graded mesh with β = 3 for each quadrilateral portion of the surface, (b) simple power-graded mesh with β = 3 for the whole surface, (c) regular contact surface discretization.

Fig. 15 shows the position of area centroid C (plus symbol), of the centre of stiffness K (cross symbol), and the orientation of both inertia and stiffness principal axis of the three case studies considered (continuous and dashed lines, respectively), obtained with a refined power-graded mesh with β = 3, n = 32 subdivisions along each side of the foundation, and, consequently, n_{el} = 768 subdivisions of the contact surface. Tab. 3 collects numerical results in terms of area centroid position, centre of stiffness position, translational and rotational stiffness for the three case studies, obtained with the refined power-graded mesh with β = 3 and n = 256 subdivisions along each side of the foundation. As expected, the centre of stiffness K does not coincide with area centroid C, and the numerical results obtained in the second and third cases are in excellent agreement with the original results obtained by Conway and Farnham [20], both in terms of C and K positions, and in terms of translational stiffness values.

Tab. 3. Numerical results in terms of area centroid position (x_C/L, y_C/L), centre of stiffness position (x_K/L, y_K/L), translational ($k_v/(E_sL)$) and rotational ($k_{\varphi x}/(E_sL^3)$, $k_{\varphi y}/(E_sL^3)$) stiffnesses for the three L-shaped foundations.

	x_C/L	y_C/L	x_K/L	y_K/L	$k_v/(E_sL)$	$k_{\varphi x}/(E_sL^3)$	$k_{\varphi y}/(E_sL^3)$
Erwin & Stephan [30]					2.067		
Present analysis	–0.167	–0.167	–0.147	–0.147	2.071	1.638	1.638
Conway & Farnham [20] #1	0.87	1.73	0.87	1.69	2.505		
Present analysis #1	0.868	1.730	0.867	1.681	2.603	4.250	11.468
Conway & Farnham [20] #2	0.83	1.75	0.84	1.70	2.461		
Present analysis #2	0.833	1.750	0.839	1.697	2.561	3.955	11.446

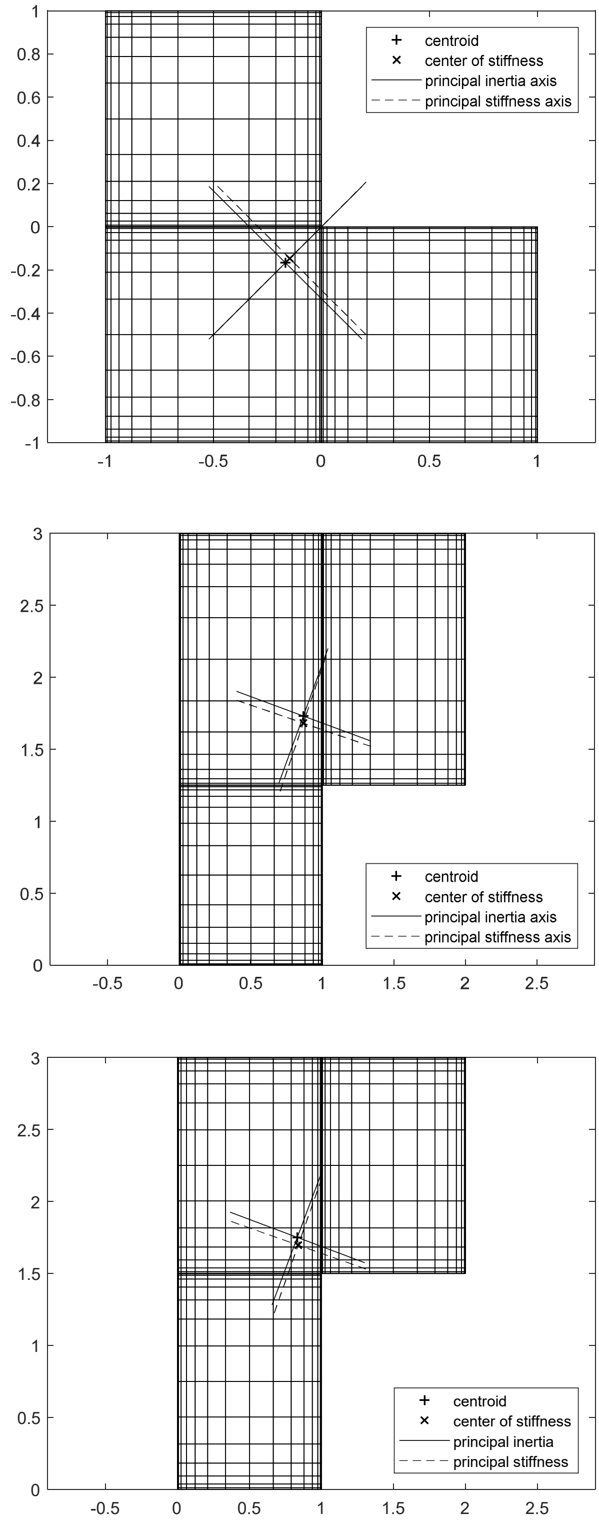

a

b

c

Fig. 15. L-shaped rigid foundations proposed by (a) Erwin and Stephan [30] and (b, c) Conway and Farnham [20] with n = 32 subdivisions along each side of the foundation and refined power-graded mesh with $\beta = 3$. Centroid position (plus symbol), centre of stiffness position (cross symbol), together with principal inertia and stiffness axis orientation, for the L-shaped rigid.

Given that the centre of stiffness position is mesh-dependent, a set of convergence tests is performed by considering the three different mesh refinements of Fig. 14 and varying the number of subdivisions along foundation sides. Results are showed in Fig. 16 in terms of the relative difference between the coordinates of the centre of stiffness and area centroid, namely $\delta x = (x_K - x_C)/x_C$, $\delta y = (y_K - y_C)/y_C$, with respect to the overall number of contact surface subdivisions n_{el}. As expected, such differences do not tend to zero, since centre of stiffness does not coincide with area centroid, and the more accurate power-graded mesh refinement with $\beta = 3$ for each quadrilateral portion of the area (Fig. 14a) turns out to be the most effective choice for determining centre of stiffness position. The less refined power graded mesh with $\beta = 3$ (Fig. 14b) turns out to have a very limited accuracy in the determination of centre of stiffness position, especially with a small number of subdivisions. The results obtained with regular surface discretization (Fig. 14c) turn out to be quite close to the most accurate ones, highlighting the importance of adopting a refined surface discretization along the entire border of the area and close to area centroid.

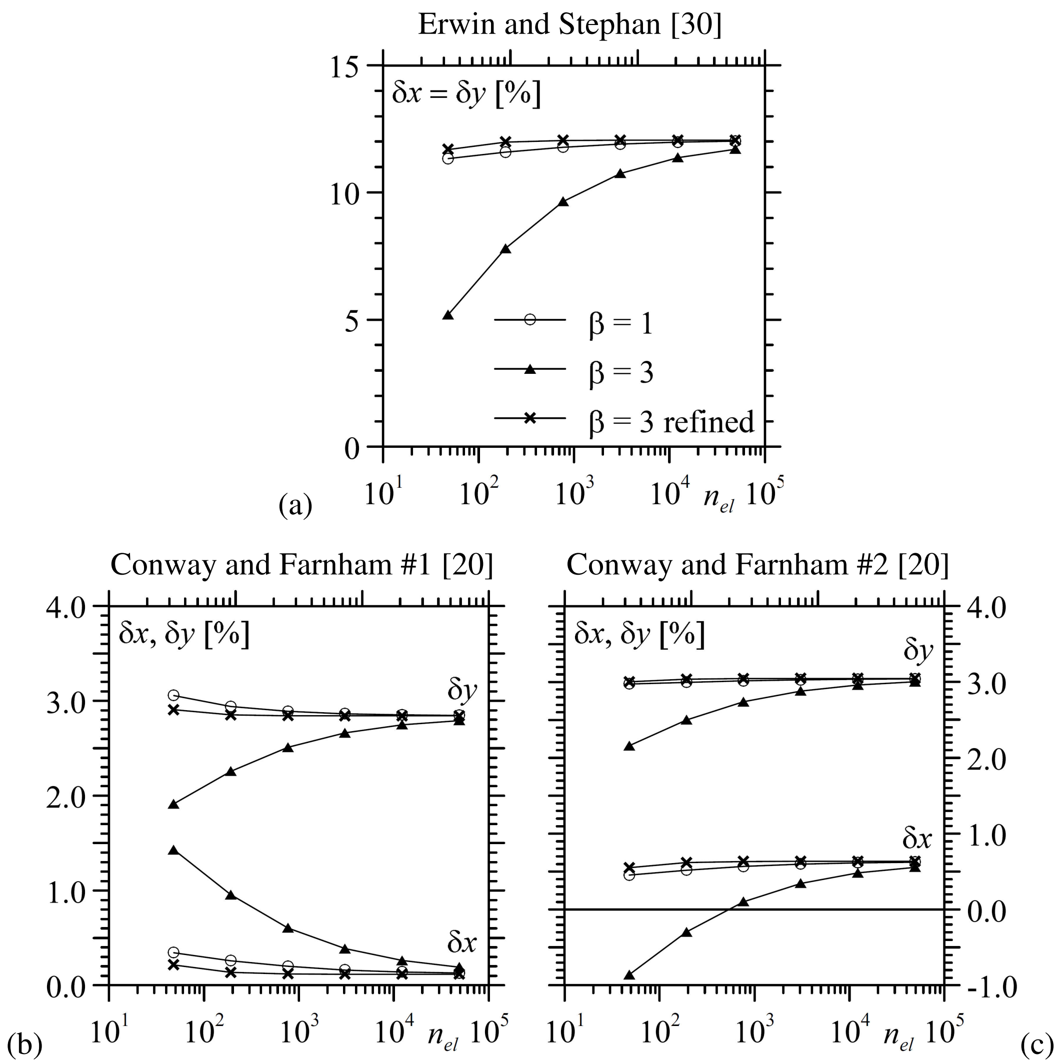

Fig. 16. Relative percentage difference between the coordinates of the centre of stiffness K and area centroid C with respect to the overall number of contact surface subdivisions n_{el} for (a) Erwin and Stephan [30], (b) Conway and Farnham #1 [20] and (c) Conway and Farnham #2 [20].

8.2 L-shaped rigid foundations subjected to forces and couples

Finally, the symmetrical L-shaped rigid foundation proposed by Erwin and Stephan [30] is subjected to four different loading conditions: a vertical force P applied at foundation centroid, a concentrated vertical force P referred to the Cartesian coordinate system (K; $\tilde{x}$, $\tilde{y}$, z) defined by the center of stiffness K and the principal axes of stiffness, and couples M_{I} and M_{II}. For the first case, contact tractions $\mathbf{r}$ and displacement $\mathbf{q}_0$ specified at the origin are determined for first by means of the system of equations (37) assuming as external load resultants $\mathbf{f} = [P, P\, x_C, P\, y_C]^{\mathrm{T}}$, then the corresponding vertical surface displacements w over the entire contact surface are calculated with Eq. (28). Alternatively, for the external load resultants referred to the Cartesian coordinate system (K; $\tilde{x}$, $\tilde{y}$, z), vertical displacement and rotations can be determined for first by means of Eq. (53), then the distribution of vertical displacement underlying the rigid foundation are prescribed by

$$w(x, y, 0) = w_K + \varphi_{\mathrm{I}}\,\tilde{y} + \varphi_{\mathrm{II}}\,\tilde{x}\,. \tag{65}$$

Making use of Eq. (50), contact tractions **r** are determined by means of Eq. (52) and Eq. (23) can be used as cross checking with the displacement field given by Eq. (65).

In the second loading condition, the external load resultant is $\mathbf{f} = [P,\ P\ x_K,\ P\ y_K]^{\mathrm{T}}$, whereas couples M_{I} and M_{II} are defined by Eq. 51a and b, respectively.

Vertical displacements and contact tractions are shown in Fig. 17 with colour maps, assuming a refined surface power-graded discretization having $\beta = 3$ and $n = 32$ subdivisions along each side of the foundation, and setting $2L$ equal to the overall width and height of the foundation. Focusing on contact tractions r, large magnitudes are obtained along the edges of the contact surface with the four load cases considered. It is worth mentioning that the concentrated force P applied at foundation centroid generates non uniform vertical displacements (Fig. 17 b), which turn out to be smaller close to the upper-right sides of the contact surface, and larger close to the lower-left corner. The second loading condition given by the vertical force P applied at foundation centre of stiffness, is of particular interest, since it generates a uniform vertical displacement, equal to $w = 0.482P/(E_sL)$ (Fig. 17 d) according to the considerations done in the previous sub-section and to those of Conway and Farnham [20]. However, contact tractions generated by P applied at foundation centre of stiffness are very close to those obtained with P applied at foundation centroid (Fig. 17 a, d). Finally, contact tractions (Fig. 17 e, g) and displacements (Fig. 17 f, h) generated by the couples M_{I} and M_{II} turn out to be linearly varying along $\tilde{y}$ and $\tilde{x}$ directions, respectively.

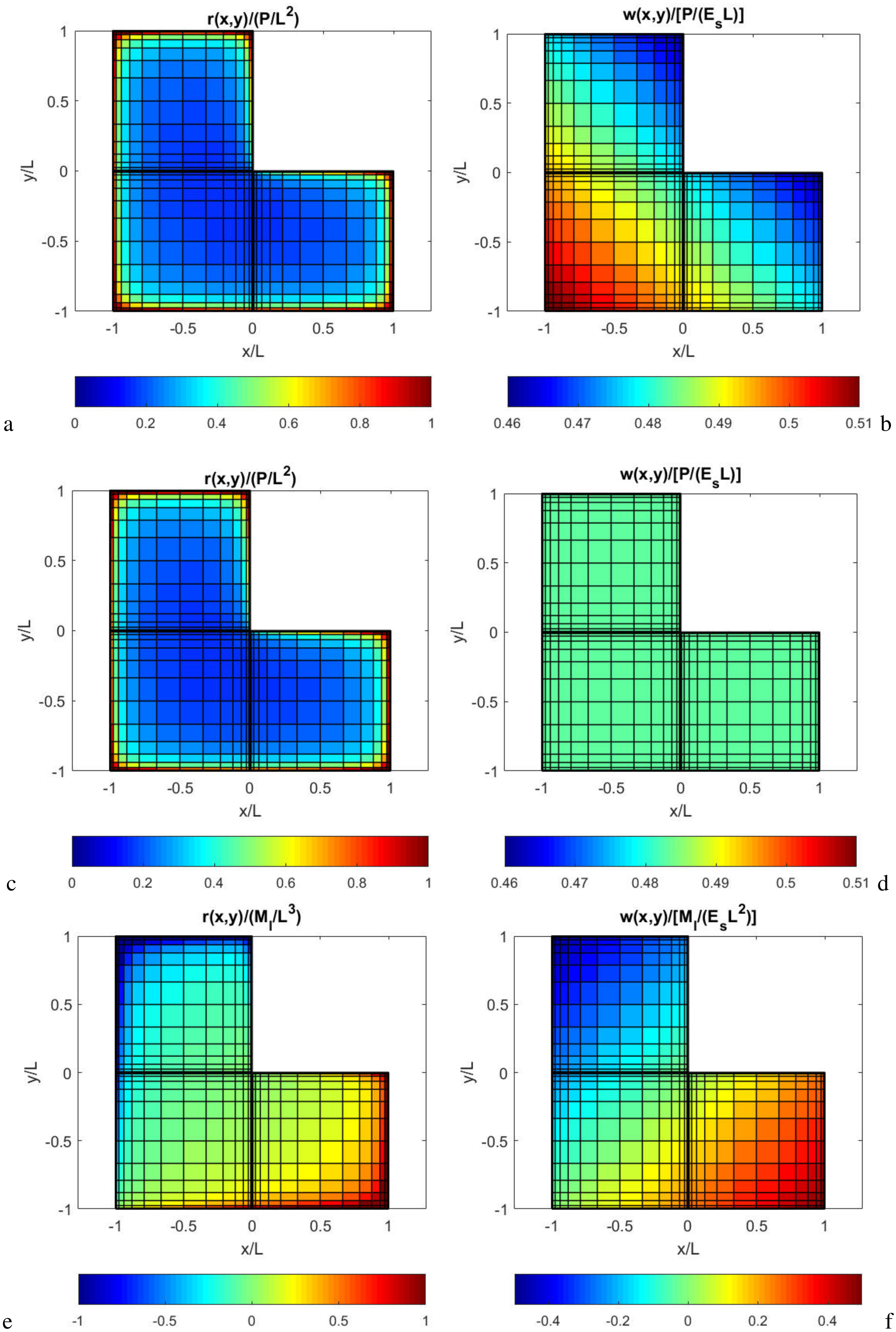
r(x,y)/(P/L^2)
w(x,y)/[P/(E$_s$L)]
r(x,y)/(M$_l$/L^3)
w(x,y)/[M$_l$/(E$_s$L^2)]
x/L
y/L
-1 -0.5 0 0.5 1
0 0.2 0.4 0.6 0.8 1
0.46 0.47 0.48 0.49 0.5 0.51
-1 -0.5 0 0.5 1
-0.4 -0.2 0 0.2 0.4
a
b
c
d
e
f

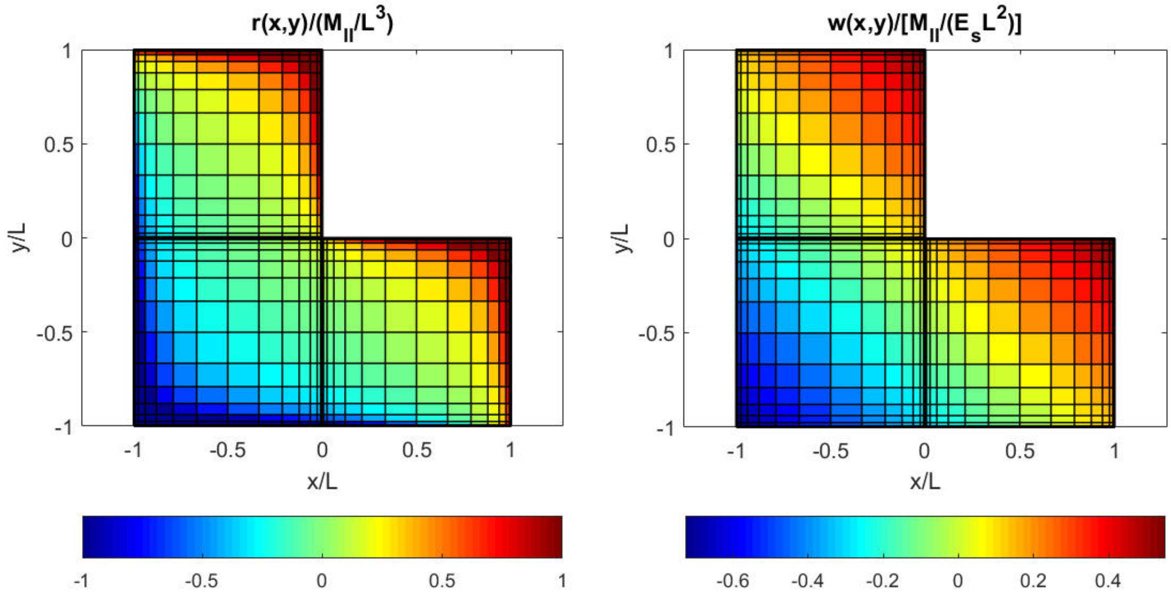

g h

Fig. 17. L-shaped rigid foundation subjected to: (a, b) a vertical force P acting on area centroid and (c, d) and at the center of stiffness K, couples (e, f) M_{I} and (g, h) M_{II}, referred to the Cartesian coordinate system (K; $\tilde{x}$, $\tilde{y}$, z). Half-space reactions (a, c, e, g) and surface vertical displacements (b, d, f, h).

CONCLUSIONS

In this work, a simple and effective Galerkin Boundary Element Method is introduced for studying flexible and rigid foundations resting on a three-dimensional elastic half-space or soil. The relationship between vertical displacements and half-space reactions is given by the Melan solution for transversely isotropic soil, reducing to Boussinesq solution for the isotropic case. The proposed numerical model discretizes both surface vertical displacements and half-space tractions by means of a piecewise constant function and by subdividing the contact surface into rectangular portions. The effectiveness of the model is demonstrated by performing several numerical tests dedicated to the determination of vertical displacements of flexible rectangular foundations subjected to vertical pressures, and to determining the translational and rotational stiffness of rigid rectangular and L-shaped foundations. Results in terms of vertical displacements and stiffness parameters turn out to be in excellent agreement with existing solutions. Furthermore, several convergence tests show that the power-graded discretization of the contact surface, characterized by small subdivisions close to the foundation edges, is more effective than a regular discretization, and in case of a L-shaped foundation, small subdivisions should be placed along the whole border of the contact area. The determination of the center of stiffness in case of unsymmetrical foundations shows that it is generally not coincident with contact surface centroid, and a concentrated vertical force has to be applied at center of stiffness in order to obtain a uniform vertical displacement of the contact surface.

Hence, the proposed GBEM to study the static behavior of a foundation resting on a half-space can be considered effective and can be coupled with traditional finite elements modelling the structure attached to the foundation. Further developments of this work will focus on the use of Eq. (37) to study the structure-footing-soil interaction problem adopting the FE-BIE coupling method, as shown in [36] for beams and frames resting on two-dimensional substrate.

ACKNOWLEDGMENTS

The present investigation was developed in the framework of the Research Program FAR 2019 of the University of Ferrara.

APPENDIX

Considering the surface Ω of the foundation subdivided into rectangular elements and adopting a piecewise constant substrate reaction, the components of the flexibility matrix $\mathbf{G}$ of the half-space are:

$$g_{ij} = \frac{1}{\pi\, E_s} \int_{y_i}^{y_{i+1}} \int_{x_i}^{x_{i+1}} \mathrm{d}\,x\, \mathrm{d}\,y \int_{\hat{y}_j}^{\hat{y}_{j+1}} \int_{\hat{x}_j}^{\hat{x}_{j+1}} \frac{\mathrm{d}\,\hat{x}\, \mathrm{d}\,\hat{y}}{d(x, y; \hat{x}, \hat{y})}$$

where the distance $d(x, y; \hat{x}, \hat{y})$ between the points (x, y, 0) and ($\hat{x}$, $\hat{y}$, 0) is reported in Eq. (5). The solution of the quadruple integral on a generic subdivision is:

$$g_{ij} = \frac{1}{\pi\, E_s} \left[\left[\left[\left[F(x, y; \hat{x}, \hat{y}) \right]_{\hat{x}_j}^{\hat{x}_{j+1}} \right]_{\hat{y}_j}^{\hat{y}_{j+1}} \right]_{x_i}^{x_{i+1}} \right]_{y_i}^{y_{i+1}}$$

$$= \frac{1}{\pi E_s} \left[\left[F(x_i, y; \hat{x}_j, \hat{y}) - F(x_i, y; \hat{x}_{j+1}, \hat{y}) - F(x_{i+1}, y; \hat{x}_j, \hat{y}) + F(x_{i+1}, y; \hat{x}_{j+1}, \hat{y}) \right]_{\hat{y}_j}^{\hat{y}_{j+1}} \right]_{y_i}^{y_{i+1}} =$$

$$= \frac{1}{\pi E_s} \{ F(x_i, y_i; \hat{x}_j, \hat{y}_j) - F(x_i, y_i; \hat{x}_{j+1}, \hat{y}_j) - F(x_{i+1}, y_i; \hat{x}_j, \hat{y}_j) + F(x_{i+1}, y_i; \hat{x}_{j+1}, \hat{y}_j)$$

$$- \left[F(x_i, y_{i+1}; \hat{x}_j, \hat{y}_j) - F(x_i, y_{i+1}; \hat{x}_{j+1}, \hat{y}_j) - F(x_{i+1}, y_{i+1}; \hat{x}_j, \hat{y}_j) + F(x_{i+1}, y_{i+1}; \hat{x}_{j+1}, \hat{y}_j) \right]$$

$$- \left[F(x_i, y_i; \hat{x}_j, \hat{y}_{j+1}) - F(x_i, y_i; \hat{x}_{j+1}, \hat{y}_{j+1}) - F(x_{i+1}, y_i; \hat{x}_j, \hat{y}_{j+1}) + F(x_{i+1}, y_i; \hat{x}_{j+1}, \hat{y}_{j+1}) \right]$$

$$+ F(x_i, y_{i+1}; \hat{x}_j, \hat{y}_{j+1}) - F(x_i, y_{i+1}; \hat{x}_{j+1}, \hat{y}_{j+1}) - F(x_{i+1}, y_{i+1}; \hat{x}_j, \hat{y}_{j+1}) + F(x_{i+1}, y_{i+1}; \hat{x}_{j+1}, \hat{y}_{j+1}) \}$$

where $F(x, \hat{x}) = F_0(x, \hat{x}) + F_1(x, \hat{x})$ and

$$F_0(x, y; \hat{x}, \hat{y}) = -\frac{[d(x, y; \hat{x}, \hat{y})]^3}{6}$$

$$F_1(x, y; \hat{x}, \hat{y}) = \frac{1}{4} |x - \hat{x}| |y - \hat{y}| \left[|y - \hat{y}| \ln \frac{d + |x - \hat{x}|}{d - |x - \hat{x}|} + |x - \hat{x}| \ln \frac{d + |y - \hat{y}|}{d - |y - \hat{y}|} \right] \quad \text{for } x \neq \hat{x},\ y \neq \hat{y}$$

$F_1(x, x; y, \hat{y}) = F_1(x, \hat{x}; y, y) = 0$

In particular

$$g_{ii} = \frac{1}{\pi E_s} \left\{ -\frac{2}{3} \left[(l_{xi}^2 + l_{yi}^2)^{3/2} - (l_{xi}^3 + l_{yi}^3) \right] + \right.$$

$$\left. + l_{xi} l_{yi} \left[l_{yi} \ln \frac{(l_{xi}^2 + l_{yi}^2)^{1/2} + l_{xi}}{(l_{xi}^2 + l_{yi}^2)^{1/2} - l_{xi}} + l_{xi} \ln \frac{(l_{xi}^2 + l_{yi}^2)^{1/2} + l_{yi}}{(l_{xi}^2 + l_{yi}^2)^{1/2} - l_{yi}} \right] \right\}$$

REFERENCES

[1] Selvadurai APS. Elastic analysis of soil-foundation interaction. Developments in Geotechnical Engineering, Amsterdam: Elsevier; 1979.

[2] Barden L. Stresses and displacements in a cross-anisotropic soil. Géotechnique 1963; 13:198–210.

[3] Atkinson J. Anisotropic elastic deformation in laboratory tests on distributed London clay. Géotechnique 1975; 25:357–374.

[4] Lin W, Kuo CH, Keer LM. Analysis of a transversely isotropic half space under normal and tangential loadings. ASME J Tribol 1991; 113:335–338

[5] Argatov I, Sabina F. Spherical indentation of a transversely isotropic elastic half-space reinforced with a thin layer. Int J Eng Sci 2012; 50:132–143.

[6] Selvadurai APS, Nikopour H. Transverse elasticity properties of a unidirectionally reinforced composite with a random fibre arrangement. Compos Struct 2012; 94:1973–1981

[7] Michell JH. The stress in an æolotropic elastic solid with an infinite plane boundary. Proc Lond Math Soc 1900; 32:247–258.

[8] Liao J, Wang C. Elastic solutions for a transversely isotropic half-space subjected to a point load. Int J Numer Anal Meth Geomech 1998; 22:425–447.

[9] Kachanov ML, Shafiro B, Tsukrov I. Handbook of elasticity solutions. Dordrecht: Kluwer Academic Publishers; 2003.

[10] Ding H, Chen W, Zhang L. Elasticity of Transversely Isotropic Materials. Dordrecht: Springer, 2006.

[11] Anyaegbunam AJ. Complete stress and displacements in a cross-anisotropic half-space caused by a surface vertical point load. Int J Geomech 2014; 14(2):171–181.

[12] Marmo F, Toraldo F, Rosati L. Transversely isotropic half-spaces subject to surface pressures. Int J Solids Struct 2017; 104–105:35–49.

[13] Boussinesq J, Application des potentials à l'etude de l'équilibre et du mouvement des solides élastiques, Gauthier Villars, Paris, 1885.

[14] Cerruti V. Ricerche intorno all'equilibrio de' corpi elastici isotropi, Reale Accademia de' Lincei, Classe di scienze fisiche, matematiche e naturali 1882; 3(13): 81–122.

[15] Johnson KL. Contact mechanics. Cambridge: Cambridge University Press; 1985.

[16] H. Lamb, On Boussinesq's problem, Proc. Lond. Math. Soc. 1902; 34, 276–284.

[17] Love AEH. The stress produced in a semi-infinite solid by pressure on part of the boundary. Philos Trans R Soc London 1929; 228(659-669):377–420.

[18] Rvachev VL. The pressure on an elastic half-space of a stamp with a wedge shaped planform, PMM 1959; 23(1):169–171

[19] Gorbunov-Posadov MI, Serebrjanyi RV. Design of structures on elastic foundations. Proceedings 5th International Conference in Soil Mechanics and Foundation Engineering. 1961; 1:643–648.

[20] Conway AD, Farnham Ka. The relationship between load and penetration for a rigid, flat-ended punch of arbitrary cross section. Int J Eng Sci 1968; 6(9):489–496.

[21] Borodachev NM. Contact problem for a stamp with a rectangular base. PMM 1976; 40(3):554–560.

[22] Brothers PW, Sinclair GB, Segedin CM. Uniform indentation of the elastic half-space by a rigid rectangular punch. Int J Solids Struct 1977; 13:1059–1072.

[23] Mullan SJ, Sinclair GB, Brothers PW. Stresses for an elastic half-space uniformly indented by a rigid rectangular footing. Int J Numer Anal Meth Geomech 1980; 4(3): 277–284.

[24] Dempsey JP, Li H. A rigid rectangular footing on an elastic layer. Technical note. Geotechnique 1989; 39(1):147–152.

[25] Bosakov SV. Solving the contact problem for a rectangular die on an elastic foundation. Int Appl Mech 2003; 39(10):1188–1192.

[26] Poulos HG, Davis EH. Elastic solutions for soil and rocks mechanics. New York: John Wiley & Sons; 1974.

[27] Whitman RV, Richart FE. Design procedures for dynamically loaded foundations. J Soil Mech Foundations Div, 1967; 93(6):169–193.

[28] Pais A, Kausel E. Approximate formulas for dynamic stiffnesses of rigid foundations. Soil Dyn Earthq Eng 1988; 7(4):213–227.

[29] Erwin VJ, Stephan EP. An improved boundary element method for the charge density of a thin electrified plate in R^3. Math Method Appl Sci 1990; 13:291–303.

[30] Erwin VJ, Stephan EP. Adaptive approximations for 3-D electrostatic plate problems. Adv Eng Software 1992; 15(3–4):211–215.

[31] D'Urso MG, Marmo F. Vertical stress distribution in isotropic half-spaces due to surface vertical loadings acting over polygonal domains. ZAMM Z Angew Math Mech 2015; 95(1):91-110.

[32] Marmo F, Rosati L. A General Approach to the Solution of Boussinesq's Problem for Polynomial Pressures Acting over Polygonal Domains. J Elast 2016; 122:75-112.

[33] Baraldi D, Tullini N. In-plane bending of Timoshenko beams in bilateral frictionless contact with an elastic half-space using a coupled FE-BIE method. Eng Anal Bound Elem 2018; 97:114–130.

[34] Tullini N, Tralli A. Static analysis of Timoshenko beam resting on elastic half-plane based on the coupling of locking-free finite elements and boundary integral. Comput Mech 2010; 45(2–3):211–225.

[35] Baraldi D, Tullini N. Incremental analysis of elasto-plastic beams and frames resting on an elastic half-plane. J Eng Mech ASCE 2019; 134(9): Article number 04017101, 1-9.

[36] Tezzon E, Tullini N, Minghini M. Static analysis of shear flexible beams and frames in adhesive contact with an isotropic elastic half-plane using a coupled FE-BIE model. Eng Struct 2015; 104:32–50.

[37] Tezzon E, Tullini N, Lanzoni L. A coupled FE-BIE model for the static analysis of Timoshenko beams bonded to an orthotropic elastic half-plane. Eng Anal Bound Elem 2016; 71:112–128.

[38] Tullini N, Tralli A, Lanzoni L. Interfacial shear stress analysis of bar and thin film bonded to 2D elastic substrate using a coupled FE-BIE method. Finite Elem Anal Des 2012; 55:42–51.

[39] Tezzon E, Tralli A, Tullini N. Debonding of FRP and thin films from an elastic half-plane using a coupled FE-BIE model. Eng Anal Bound Elem 2018; 93:21-28.

[40] Tullini N, Tralli A, Baraldi D. Stability of slender beams and frames resting on 2D elastic half-space. Arch Appl Mech 2013; 83(3):467–482.

[41] Baraldi D. Static and buckling analysis of thin beams on an elastic layer. Comp Mech Comput Appl Int J 2019. 10(3):187–211.

[42] Tullini N, Tralli A, Baraldi D. Buckling of Timoshenko beams in frictionless contact with an elastic half-plane. J Eng Mech 2013; 139(7):824–831.

[43] Gurtin ME, Sternberg E. Theorems in linear elastostatics for exterior domains. Arch Ration Mech Anal 1961; 8:99–119.

[44] Costabel M. Boundary integral operators on Lipschitz domains: Elementary results. SIAM J Math Anal 1988; 19:613–626.

[45] Dauge M. Elliptic boundary value problems on corner domains. Lecture Notes in Mathematics. Springer-Verlag. 1988.

[46] Ainsworth M, McLean W, Tran T. Diagonal scaling of stiffness matrices in the Galerkin boundary element method. ANZIAM J 2000; 42(1): 141–150.

[47] Graham IG, McLean W. Anisotropic mesh refinement: the conditioning of Galerkin boundary element matrices and simple preconditioners. SIAM J Numer Anal 2006; 44(4): 1487–1513.

[48] Guzina BB, Pak RYS, Martínez-Castro AE. Singular boundary elements for three-dimensional elasticity problems. Eng Anal Bound Elem 2006, 30:623–639.

[49] Eskandari-Ghadi M, Mehdizadeh D, Morshedifard A, Rahimian M, A family of exponentially-gradient elements for numerical computation of singular boundary value problems. Eng Anal Bound Elem 2017; 80:184–198.

[50] Timoshenko SP, Goodier JN. Theory of elasticity. New York: McGraw-Hill; 1951.

[51] Morrison JA, Lewis JA. Charge singularity at the corner of a flat plate, SIAM J Appl Math 1976; 31:233–250.

[52] Li H, Dempsey JP, Unbonded Contact of a Square Plate on an Elastic Half-Space or a Winkler Foundation. J Appl Mech – ASME 1988; 55:430–436.

[53] Sinclair GB. Stress singularities in classical elasticity–II: Asymptotic identification. Appl Mech Rev 2004; 57(5):385–439.

[54] Rayleigh JW. Theory of Sound. New York: Dover Publications; 1929.

[55] Vesic AB. Bending of beams on isotropic elastic medium. J Eng Mech Div - ASCE 1961; 87(EM2):35–53.

FIGURE CAPTIONS

Fig. 1. Flat foundation resting on an elastic half-space.

Fig. 2. Examples of power-graded meshes for a square with unitary side length varying the number of element n and grading exponent β.

Fig. 3. Elastic half-space loaded by a constant pressure p over a rectangular surface.

Fig. 4. Relative errors δw for displacements evaluated at points (a) O, (b) C and (c, d) M, N.

Fig. 5. Dimensionless vertical displacements w^* (a) along the x-axis and (b) along the diagonal due to a uniform pressure over a square surface.

Fig. 6. Dimensionless vertical displacements w^* beneath a rectangular area due to a uniform pressure (continuous lines for present analysis, cross symbols for Love's solution).

Fig. 7. Rigid rectangular foundation resting on an elastic half-space.

Fig. 8. Dimensionless normal traction due to a vertical force (a) along x-axis, (b) at the midpoint of the edge parallel to y-axis, (c) along the diagonal and (d) at the corner.

Fig. 9. Dimensionless normal traction due to a vertical force. Square surface is subdivided with a power graded mesh having 16 elements for each side and $\beta = 3$.

Fig. 10. Relative errors for k_v varying (a) the number of subdivisions along each surface side and (b) the total number of boundary elements.

Fig. 11. Relative errors for $k_{\varphi x}$ varying (a) the number of subdivisions along each surface side and (b) the total number of boundary elements.

Fig. 12. Dimensionless vertical stiffness c_{vf}, c_{vr} and rotational stiffness $c_{\varphi x}$ of a rigid rectangular foundation varying L_1/L_2 ratio. (continuous lines for present analysis, cross symbol for Whitman and Richart (1967) data).

Fig. 13. L-shaped rigid foundations proposed by (a) Erwin and Stephan [30] and (b, c) Conway and Farnham [20].

Fig. 14. L-shaped rigid foundations having 8 subdivisions along x and y directions, and with (a) refined power-graded mesh with $\beta = 3$ for each quadrilateral portion of the surface, (b) simple power-graded mesh with $\beta = 3$ for the whole surface, (c) regular contact surface discretization.

Fig. 15. L-shaped rigid foundations proposed by (a) Erwin and Stephan [30] and (b, c) Conway and Farnham [20] with $n = 32$ subdivisions along each side of the foundation and refined power-graded mesh with $\beta = 3$. Centroid position (plus symbol), centre of stiffness position (cross symbol), together with principal inertia and stiffness axis orientation, for the L-shaped rigid.

Fig. 16. Relative percentage difference between the coordinates of the centre of stiffness K and area centroid C with respect to the overall number of contact surface subdivisions n_{el} for (a) Erwin and Stephan [30], (b) Conway and Farnham #1 [20] and (c) Conway and Farnham #2 [20].

Fig. 17. L-shaped rigid foundation subjected to: (a, b) a vertical force P acting on area centroid and (c, d) and at the center of stiffness K, couples (e, f) M_{I} and (g, h) M_{II}, referred to the Cartesian coordinate system (K; $\tilde{x}$, $\tilde{y}$, z). Half-space reactions (a, c, e, g) and surface vertical displacements (b, d, f, h).

TABLE CAPTIONS

Tab. 1. Dimensionless vertical stiffness c_{vf} for flexible rectangular foundation.

Tab. 2. Dimensionless vertical stiffness values for rigid square foundation.

Tab. 3. Numerical results in terms of area centroid position (x_C/L, y_C/L), centre of stiffness position (x_K/L, y_K/L), translational ($k_v/(E_sL)$) and rotational ($k_{\varphi x}/(E_sL^3)$, $k_{\varphi y}/(E_sL^3)$) stiffnesses for the three L-shaped foundations.